Chapter 7

Quality of Service and Routing Performance Evaluation for IEEE 802.15.6 Body Sensor Networks Using an Accurate Physical Layer

J.-M. Dricot, S. Van Roy, Ph. De Doncker, and A. Nonclercq
Université Libre de Bruxelles
M. Rinaudo
Université Libre de Bruxelles and University of Parma
Gianluigi Ferrari
University of Parma

Contents

7.1 Introduction

7.1.1 Motivation

The current increase in health care spending is one of the many challenges that health care systems have to face. It has led to concerns about long-term sustainability [1]. For instance, inflation-adjusted per capita health expenditures in the United States—which devotes the largest share of its gross domestic product to health care (17.6% in 2009)—have increased from approximately $809 in 1960 to $7375 in 2009, with an average annual growth rate of approximately 4.7% [2]. Another challenge is the aging of the population, which is also accounting for the increase in health care costs. It is expected that the number of persons with ages 60 years or older will increase from 688 million in 2006 to almost 2 billion by 2050, at which point (for the first time in human history) the population of older persons will be larger than the population of children [3]. Those two challenges highlight the need for better health system efficiency.

Recent advances in ultra-low power wireless sensors have fostered research in the field of body-centric wireless networks, also referred to as *body area networks* (BANs) [4–7]. In these networks, a set of nodes (called sensors) is deployed on the human body. They aim at monitoring and reporting several physiological values, such as blood pressure, breath rate, skin temperature, or heart beating rate.

This chapter addresses the development of a specific framework for the accurate computation of the network topology (i.e., routing) suitable for medical applications. First, a comprehensive and detailed analytical framework for BAN performance evaluation is developed, obtaining closed-form expressions for the link probabilities of outage in the context of multiuser communications. This framework encompasses the effects of environment, topology, and traffic intensity.

In the remainder of this section, state-of-the-art medical sensor network applications are presented. The medical best practices and standards in use are presented and the effect of wireless sensor networking on modern medicine is extensively detailed. In Section 7.2, an accurate channel model for on-body communications, based on an extensive measurement campaign using

high-accuracy and large bandwidth spectrum analyzers, is presented. In Section 7.3, a link–layer performance is evaluated with a computation of the link probability of success when using multisensor communications. The derivations take into account sensor activity (through its probability of transmission) and the effect of the environment as well. In Section 7.4, the link-level throughput and the delay are defined. The distinction between random access networks (i.e., slotted ALOHA) and time division multiple access networks (i.e., TDMA) is described. Next, in Section 7.5, the routing performance is analyzed and a novel framework for the computation of the optimal BAN topology is introduced. Section 7.6 concludes this chapter and presents open research questions.

7.1.2 Sensor Networks and Their Application in Modern Medicine

BANs allow continuous monitoring of patients at home—compared with short-time monitoring at the hospital and, besides a traditional follow-up of a given pathology for a patient, they may also help in prevention medicine, early detection of pathologies, population screening, monitoring of good adhesion to treatment guidelines, etc. The increase in interest for wearable monitors and Holter monitors may be seen as a first step toward BANs, as they also allow those features. However, current systems are usually cumbersome and wires are impractical. Furthermore, data processing and analysis are usually performed offline, making such devices not well-suited for continuous monitoring [8]. BANs provide a way to overcome those limitations. A BAN may be used in different types of frameworks, including monitoring patients with chronic disease, patients in hospitals, elderly patients at home, or even continuous monitoring of patients in any kind of environment. In particular, it can be used for numerous applications such as arrhythmias, hypertension, diabetes, elderly patient monitoring, and drug delivery through integrated feedback systems (see Aziz et al. [9] for review). Although most applications are focused on surface sensors, some also allow an implanted distributed sensor network. BION, for instance, proposes neural prosthetic interfaces that allow multichannel systems to be assembled from single-channel micromodules [10]. Besides clinical application, BANs may also be instrumental in various other applications, including human–computer interfaces and gaming [11].

As many applications and types of BANs appear, it is important to define some key terminologies and to propose a classificatory framework providing a general understanding of the technical aspects related to these systems [12]. Here, we will define only a few. A BAN may be defined as "a network of communicating devices worn on, around, or within the body, which is used to acquire health-related data and provide mobile health services to the user" [12]. The BAN may be composed of noninvasive (worn on the body) or invasive (worn in the body) sensors and actuators, other network nodes placed around the patient (such as an external sensor informing of the environment of the patient, a video camera informing the posture of the patient, or a screen providing feedback to the patient), as well as a base unit, which are communicating together (intra-BAN communication). Furthermore, extra-BAN communication usually also exists, allowing the system to communicate with a remote user, for instance, a health professional, through a central server system called BackEnd. Numerous BAN systems have been proposed (see, for instance, Aziz et al. [9] and Yuce [13] for reviews), including various physiological monitoring systems for individual or group use in medical centers or in home care [13], computer-assisted physical rehabilitation [14], implantable neural recording [15], and heart activity monitoring [16]. Many systems aiming to monitor patient physiological data share common features and therefore could also be used for a wide range of applications with few modifications.

Building a successful BAN seems to be a challenging task. Most telemedicine applications remain in the pilot phase and never reach proper use in daily practice [17–19]. To be successful, the major determinants may be divided into five classes [19]: (1) technology, (2) acceptance, (3) financing, (4) organization and, (5) policy and legislation. We will address some of the major related challenges.

Biomedical signal acquisition is a difficult task and has been greatly studied [20–23]. The difficulty usually comes from the low amplitude that physiological potentials such as electrocardiographic, electromyographic, or electroencephalographic potentials may show, which makes them sensitive to the noise generated by the device, electrical interference from the surroundings, and artifacts. It is estimated that in most bioelectric measurements, the overall disturbance level should be lower than 1 to 10 μV peak-to-peak [20].

Interferences are due to various unwanted couplings [20]. A capacitive coupling between the patient, the mains, and the earth causes interference currents flowing through the body. Similarly, both the amplifier and the wires connecting the electrodes to the amplifier are capacitively coupled to the mains and to the earth, causing parasitic currents. Magnetically induced interferences are also present due to the loop formed by the measurement wires. By nature, a BAN shows short wires connecting the electrodes and the amplifier, reducing the parasitic coupling; in this regard, it is less prone to interferences.

The noise generated by the device is mainly due to the first stages of the front-end, composed of the electrodes and the amplifier stage. The noise of typical Ag–AgCl electrodes is estimated to range from 1 to 15 μVRMS for electrodes placed on the body surface in a 0.5 to 500 Hz band-pass [24]. Much effort has been made by manufacturers to decrease the input noise of instrumentation amplifiers, even for the low frequencies needed, so that levels lower than 1 μV peak-to-peak may be reached for the typically required bandwidths. Finally, artifacts may affect the quality of the recording. Artifacts may be divided into two categories. First, physiological artifacts could be due to the biopotentials generated by the patients themselves, interfering with the acquisition of the physiological signal of interest. Second, nonphysiological artifacts are due to transitory perturbation such as motion artifacts, impurities, and deterioration of the electrodes and electrostatic artifacts. Among these, motion artifacts are probably one of the most problematic because they are frequent and are not confined to a small spectral band [25,26].

Patient safety, of course, is an issue of major importance for a BAN, as for any other medical device. IEC 60601 International Standards, published by the International Electrotechnical Commission, lists the requirements regarding the safety and effectiveness of medical electrical equipment. Compliance with the IEC 60601 International Standards is a recognized step toward medical device approval in nearly all markets across the world, including the United States, Europe, Canada, Japan, Australia, and other countries [27]. Besides all conventional issues related to safety, the radiation issue that a BAN implies through its communication and the long-term consequences of this radiation on the body should be assessed, particularly in the case of implantable sensors [9].

Safety is of course mandatory under normal operational conditions, but this is also true under first fault conditions. In this regard, even if a medical device may fail, it should do so safely. Besides, it is important to be able to detect a fault in the system when it occurs, to be able to interrupt its use, and to avoid the occurrence of another fault that could lead to a risk for the patient. Fault detection in BAN has been studied for many years [28], and robust fault detection should be designed for any BAN. The concept of essential performance, that is, the performance necessary to achieve freedom from unacceptable risk, has received much attention in the last few years and its application lead to a change in the title of the IEC60601-1 publication [29] from "Medical

electrical equipment, Part 1: General requirements for safety" in the second edition, to "Medical electrical equipment, Part 1: General requirements for basic safety and essential performance" in the third edition (IEC60601-1) [30]. Essential performance is directly related to patient safety as one should understand it by considering whether its absence or degradation would result in an unacceptable risk.

This concept is clearly illustrated in applications such as life-supporting devices for which accuracy is vital, medication administered in a closed-loop system for which overdosing is unacceptable, or preimpact fall detection for which malfunctioning may imply major injury [9,31]. Besides those obvious examples, another example of essential performance is the "correct output of diagnostic information from medical equipment that is likely to be relied upon to determine treatment, where incorrect information could lead to an inappropriate treatment that would present an unacceptable risk to the patient" (IEC60601-1) [30]. Because the purpose of the large majority of medical equipment is to help the medical professional in realizing a diagnostic, such an example nearly always applies. Therefore, the data acquired from the BAN should always be accurate or, at least, it should be made clear when inaccurate information occurs to make sure that it would never lead to an inappropriate treatment. There are many types of inaccurate information, including data that is unavailable, incorrect, or with incorrect timing.

Focusing on BANs, wireless communication is prone to different types of problems leading to inaccurate data, including interference caused by other wireless devices that share identical channels, harsh network environments, low batteries, and unusual motions [28,32]. Various methods have been proposed to achieve robust data transmission, including packet retransmission [13,33], use of a multipath network to avoid disrupted links [9,34], and multicast or broadcast-based routing schemes [35,36]. Local data storage at the node level [26] may also be an option to backup potential data loss during transmission, at the cost of a more complex data transmission (or offline data download), and larger data storage components.

Data synchronization has great importance, as it may affect the synchronization of two physiological signals, or even the integrity of the whole data set. In general, the synchronization timing error between two signals is small in BANs when compared with the length of most physiological patterns. However, one should also take into account that many medical definitions, which affect the corresponding diagnostics, are based on the latency between two physiological events and use a fixed threshold. For instance, let us consider that the occurrence of two physiological events, concurrent within a 5-s window, is considered pathological. Then let us consider that, for a given patient, those two physiological events occur exactly with a 5-s interval and therefore should be considered pathological. In this case, even the smallest synchronization timing error that would increase the time interval between the two events would imply the wrong assumption that no pathological event occurred. This said, one should be able to stand back when analyzing such a recording, and it is assumed that a medical professional would have the insight needed to do so, but automatic signal processing may not. Many algorithms have been proposed to provide time synchronization in BAN, usually achieving average synchronization timing errors of less than 30 μs.

An artifact is also likely to corrupt data [28,32]. Besides the traditional signal processing often proposed to detect and remove artifacts, BAN context awareness may help account for artifacts [9]. Motion artifacts, one of the most problematic types of artifact [25,26], may be detected using motion analysis systems based on kinematic sensors [26,37,38].

As for any medical device, electromagnetic compatibility is an important issue that needs to be assessed, both for the unintentional generation and reception of electromagnetic energy. The aim is to ensure that the BAN does not interfere with other devices or is not disturbed by

other devices through spurious emission and absorption of electromagnetic interference. Various standards have been published, depending on the country of use, detailing the technical and performance requirements to which the devices will be tested (e.g., IEC60601-1-2 2007). Compared with traditional wired monitoring devices, the use of wireless communication makes BAN more prone to electromagnetic interference emission and less immune to it, so this issue should be assessed carefully.

Privacy and security issues also need to be considered. The wireless nature of BAN makes them more prone to various security threats. This issue is common to all wireless networks, but the clinical use usually made by the BAN makes it most critical, and has therefore been heavily investigated for those applications [35,39,40]. Threats and attacks include data modification, impersonation attack, eavesdropping, and replaying (the attacker resends a piece of valid information), and security mechanisms include data encryption, data integrity and data origin authentication, authentication, and freshness protection [39]. Various possible solutions for security methods in BAN have been proposed (e.g., see articles by Ng et al. [40] and Dağtas et al. [41]).

Comfort is one of the key features that may be greatly improved by using a BAN. Traditionally, the patient is connected to the (usually large) monitoring device through wires, which reduces the patient's comfort and mobility [11]. Using a BAN is therefore beneficial, as those wires are removed. However, to keep this advantage, the BAN nodes should be small, even forgettable to the user, and allow autonomic donning and doffing [18]. Besides BAN, other architectures also allow the removal of those undesirable wires. For instance, another option is the use of a wearable textile interface that is implemented by integrating sensors, electrodes, and connections in fabric form [42].

Finally, power consumption, due both to data acquisition and transmission, is a key issue in BAN. It has a direct effect on comfort as it characterizes the trade-off between the size of the battery embedded in each node and its battery life. Both low power data acquisition [43–45] and low power data transmission [11,15,46] have been proposed. An interesting new trend is the use of power scavenging to enhance battery life, using surrounding energy sources such as thermal body heat [26] and body movement [47]. Another option, aiming to reduce data transmission power consumption, is to perform data processing (such as feature extraction) within the BAN node, so that only relevant information is transmitted [8]. However, two drawbacks of this method are the increase in power consumption due to data processing, and the potential loss of information occurring during the processing.

At least 10% of the population suffers from a sleep disorder that is clinically significant and of public health importance. To detect and assess sleep disorders, it is common to use a polysomnogram, a medical tool monitoring a wide variety of physiological parameters related to sleep.

Although polysomnography is traditionally performed at the hospital, there is a trend in performing sleep monitoring at home. The benefits over traditional polysomnography include a more comfortable patient's sleep, which is more indicative of his/her normal sleep, a cost that is substantially less expensive (25%–30% of the cost of traditional polysomnography), shorter waiting lists, etc. [48,49]. Even if there is still a debate regarding the validity of available home sleep testing devices, various authors report that the outputs from polysomnography and home sleep tests are not much different [49]. Another issue associated with traditional polysomnography is the long wires connecting the sensors, which can create discomfort and result in cable movement artifacts [11,49].

7.1.3 Medical Scenario of Interest

The portability and wireless nature of the BAN makes it highly suitable for home sleep monitoring. In this sense, various wireless devices and BAN used in sleep monitoring have been previously proposed [11,50,51]. Following those, we propose a BAN used for sleep monitoring. The choice of recorded physiological parameters and positioning of sensors is given in Table 7.1. This is believed to be typical because it is based on technical recommendations such as those made by Patel et al. [49] Chokroverty [52], Quan et al. [53], Patil [54], and Iber et al. [55], and according to the specifications of major manufacturers. The distribution of sensors is represented in Figure 7.1 and will serve as the basis for the performance analysis detailed in Sections 7.4 and 7.5.

Table 7.1 Specifications of a Typical Neurophysiologic Monitoring Device

Acronym	*Name*	*Bandwidth (bits/s)*	*Location*
PHONO	Sound probe	16,000	Neck
EEG	Electroencephalograph	25,600	Head
EOG	Electro-oculogram	6,400	Head
EMG1	Electromyograph	3,200	Chin
EMG2	Electromyograph	3,200	Left leg
EMG3	Electromyograph	3,200	Right leg
ECG	Electrocardiogram	3,200	Heart
NFL	Nasal/oral airflow	600	Nose/mouth
PAP	Positive airway pressure monitoring	600	Nose/mouth
POS	Position	600	Thorax
VAB	Plethysmograph	600	Abdomen
VTH	Plethysmograph	600	Thorax
SPO2	Arterial hemoglobin saturation	600	Finger
PR	Pulse rate	600	Finger
PTL	Plethysmograph	600	Finger
PTT	Pulse transit time	600	Finger
LIGHT	Light	600	Thorax

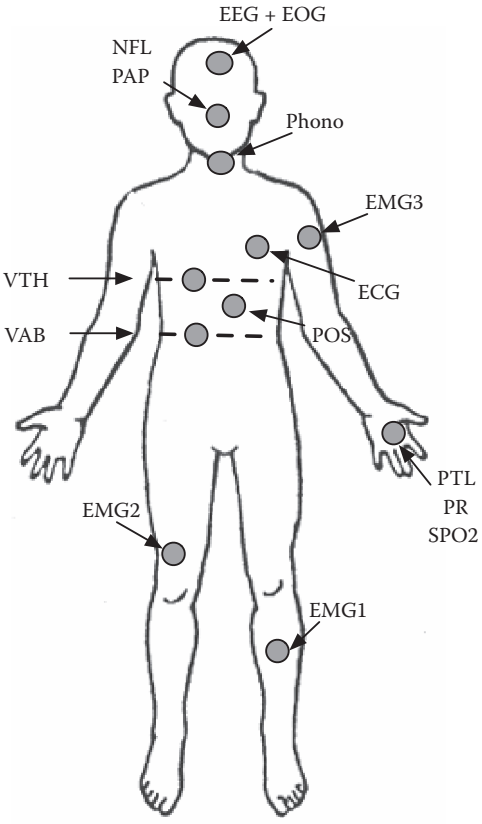

Figure 7.1 Physical model of the medical scenario.

7.2 Physical Channel Modeling for On-Body Communications

To build an accurate model for the on-body propagation, a Rohde & Schwartz ZVA-24 vector network analyzer was used to capture the complex-valued frequency-domain transfer function between 3 and 7 GHz, with a frequency step of 50 MHz. Omnidirectional Skycross SMT-3T010M ultrawideband antennas were used during the entire measurement campaign. Their small size (13.6 mm × 16 mm × 3 mm) and low profile characteristics precisely match the body sensor requirements. These antennas were separated from the body skin by about 5 mm to ensure a return loss value of $S_{11} \leq -9$ dB. Finally, low-loss and phase-stable cables interconnect all components and the IF bandwidth was set to 100 Hz to enlarge the dynamic range to about 120 dB.

The experimental scenario is presented in Figure 7.2 and can be described as follows. The measurements were carried out at approximately 94 cm of the waist of a man (1.87 m, 83 kg) whose body was in a standing position, arms hanging along the side. The transmitter antenna was placed around the body at a distance d from the receiver antenna, which is located at the middle axis of the torso.

Figure 7.3 (obtained from our previous work [56,57]) presents the power delay profile and channel gain between two nodes. This information is then used to derive a very accurate propagation model that accounts for the average received power, the statistical variations of the signal

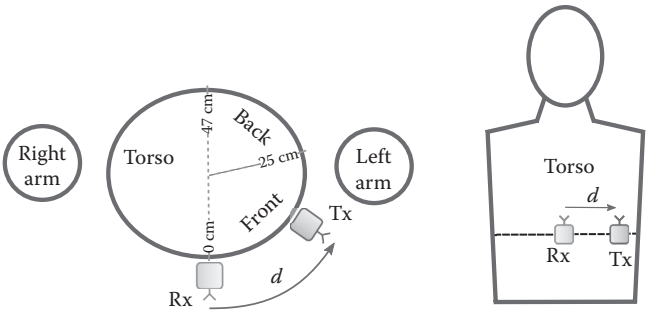

Figure 7.2 Possible positions of a transmitter–receiver pair in a BAN.

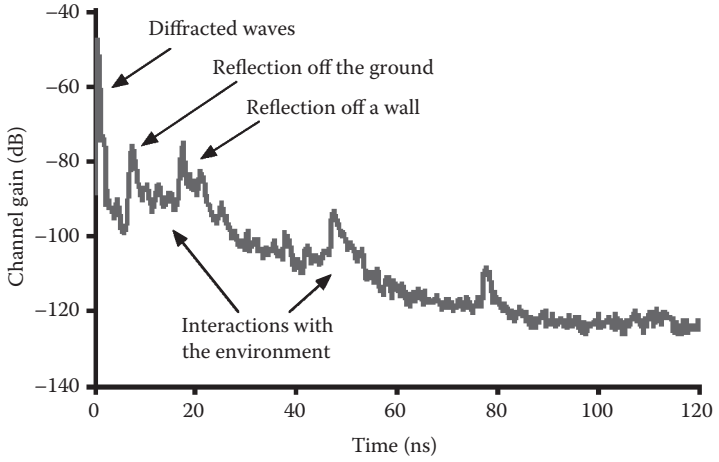

Figure 7.3 Power delay profile as a function of the time in an indoor environment and for $d \leq 25$ cm (body front).

(i.e., shadowing, movements of the limbs, etc.), and the effect of the environment (indoor or outdoor) [57].

The conclusions of this extensive measurement campaign, also highlighted by the model studied by Van Roy et al. [58], can be summarized according to three points. First, there is propagation through the body. However, when high transmission frequencies are considered, the attenuation undergone by these waves is relevant and the corresponding contribution can be neglected.

A second mechanism corresponds to guided diffraction around the body. This mechanism is consistent with surface wave propagation and its properties depend on the body specific characteristics.

Finally, the last propagation contribution comes from the surrounding environment. More precisely, the third propagation mechanism originates from reflections off the body limbs (arms and legs) and the surrounding objects (walls, floor, and ceiling). Obviously, this mechanism is observed only in an indoor environment.

Based on an extensive measurement campaign, we now present accurate statistical models corresponding to the propagation mechanisms described above.

7.2.1 On-Body Propagation (Guided Diffraction)

As previously emphasized by Ryckaert et al. [56] and Van Roy et al. [57], the average received power (on the decibel scale) is the following linearly decreasing function of distance:

$$\mathbb{E}[\mathbf{P}(d)] = P + L_{\text{ref}} + 10\gamma(d - d_{\text{ref}}) \quad d \geq d_{\text{ref}} \tag{7.1}$$

where $\mathbf{P}(d)$ is the instantaneous received power (dimension, W) at distance d (dimension, m), P the transmit power (dimension, W), d_{ref} is a reference distance (dimension, m), L_{ref} is the gain at the reference distance (adimensional, in decibels), and γ is a suitable constant (dimension, m^{-1}). For instance, typical experimental values for these parameters are $d_{\text{ref}} = 8$ cm, $L_{\text{ref}} = -57.42$ dB, and $\gamma = -124$ dB/m [57]. The average received power, in linear scale, can then be expressed as follows:

$$\mathbb{E}[\mathbf{P}(d)] = P \cdot L(d) \quad d \geq d_{\text{ref}} \tag{7.2}$$

with

$$\begin{aligned} L(d) &= \underbrace{10^{(L_{\text{ref}} - 10\gamma d_{\text{ref}})/10}}_{\triangleq L_0} \cdot 10^{\gamma d} \\ &= L_0 10^{\gamma d} \; d \geq d_{\text{ref}} \end{aligned} \tag{7.3}$$

where L_0 is a function of L_{ref}, d_{ref}, and γ.* In Figure 7.4a, the loss L is shown as a function of the distance, considering narrowband transmissions at 5 GHz. More precisely, in Figure 7.4a, experimental measurements (circles) and their linear interpolation (solid line) are shown. Finally, using Equation 7.3 in Equation 7.2, one obtains:

$$\mathbb{E}[\mathbf{P}(d)] = PL_0 10^{\gamma d}. \tag{7.4}$$

Although Expression 7.4 characterizes the average value, it does not provide insights into the instantaneous distribution of the received power. In the study by Van Roy et al. [57], it has been experimentally observed that the on-body propagation channel is characterized by slow large-scale fading (i.e., shadowing). More precisely, the instantaneous received power at distance d can be expressed as follows:

$$\mathbf{P}(d) = PL_0 10^{\gamma d} \mathbf{X}$$

where $\mathbf{X}$ is a random variable (RV) that depends on the channel characteristics. As shown in the study by Takada et al. [59], and as confirmed in our measurements, $\mathbf{X}$ has a log-normal distribution† with parameters μ and σ, where σ_{dB} typically ranges from 4 to 10 dB, μ_{dB} is the average path loss on the link (dimension, dB). Because the loss is accounted for by the term $L(d)$, it follows that $\mu_{\text{dB}} = 0$ dB and the cumulative distribution function (cdf) of $\mathbf{X}$ reduces to the following:

$$F_{\mathbf{X}}(x; 0, \sigma) = \frac{1}{2} - \frac{1}{2}\text{erf}\left(\frac{-10\log_{10} x}{\sigma\sqrt{2}}\right)$$

* Note that, even though Equation 7.3 holds for $d \geq d_{\text{ref}}$, L_0 can be intuitively interpreted as the (extrapolated) gain (adimensional, linear scale) at distance $d = 0$. In other words, L_0 takes into account the loss due to antenna emission.

† Note that we use the $\log_{10}$ variant of the log-normal because the widely used shadowing model uses an additive Gaussian variation expressed in decibels.

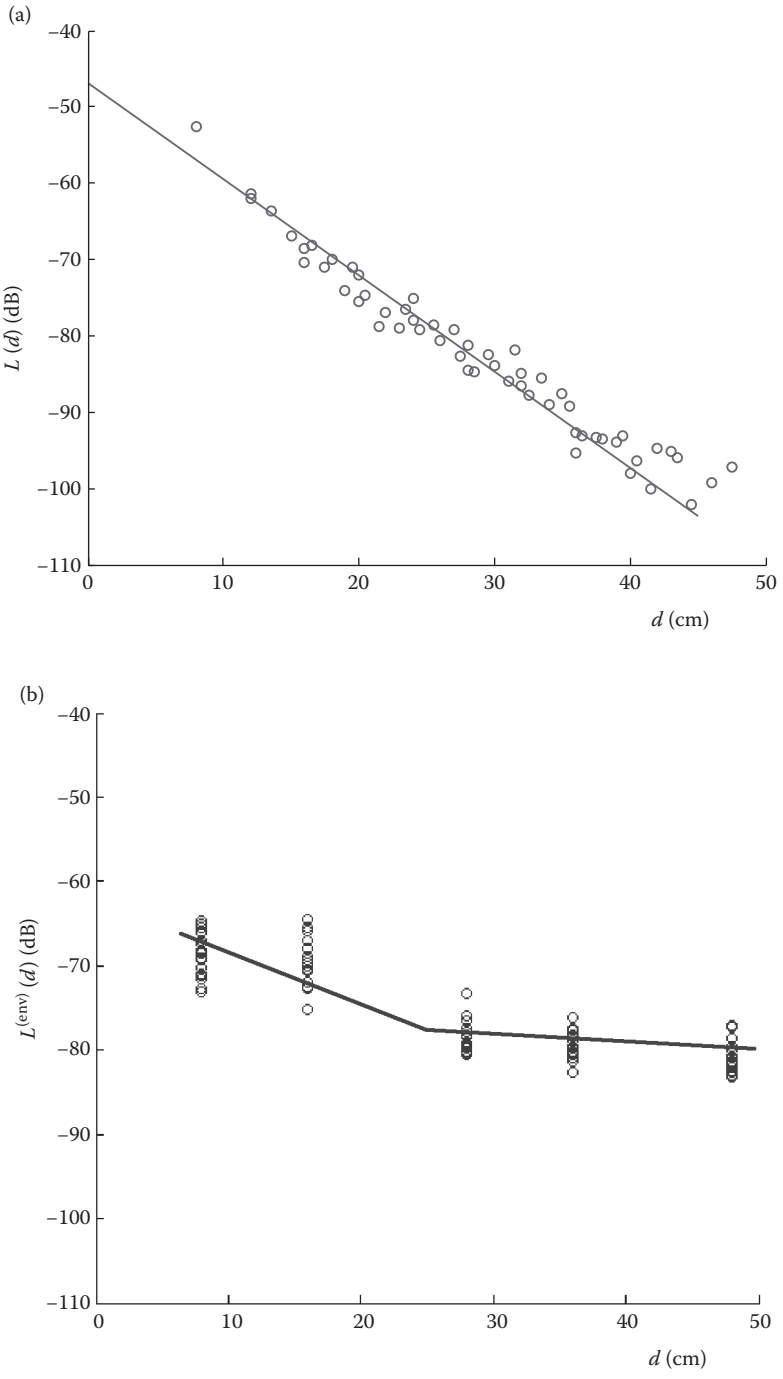

Figure 7.4 Propagation loss as a function of the distance: (a) on-body propagation and (b) propagation through reflections off the environment. In both cases, experimental results (circles) and their linear (or piecewise linear, in b) interpolations are shown (solid line).

with the following corresponding probability density function (pdf):

$$f_X(x;0,\sigma) = \frac{10}{(\ln 10)\, x\, \sqrt{2\pi}\sigma} \exp\left\{ -\frac{(10\log_{10} x)^2}{2\sigma^2} \right\}. \tag{7.5}$$

7.2.2 Reflections Off the Environment

The second significant propagation mechanism originates from multiple reflections off the environment. A substantial measurement campaign has shown that the contribution of the environment can be considered, on average, as an additive, constant power when the transmission distance is significant (i.e., when $d > 25$ cm). The obtained results are shown in Figure 7.4b, the power received with reflections from the surrounding environment is shown as a function of the distance. It can be observed that when $d > 25$ cm, the value of the loss is, on average, approximately 78 dB. More precisely, for $d > 25$ cm, the average value of the received power can be expressed, in logarithmic scale, as follows:

$$\mathbb{E}[\mathbf{P}_{\text{env}}] = P_{\text{env}} \triangleq P + L_{\text{dB}}^{(\text{env})} \tag{7.6}$$

where P is the transmit power and $L_{\text{dB}}^{(\text{env})} \simeq -78$ dB. Alternatively, the average received power can be expressed in linear scale as

$$\mathbb{E}[\mathbf{P}_{\text{env}}] = P_{\text{env}} \triangleq P \cdot L^{(\text{env})} \tag{7.7}$$

where $L^{(\text{env})} = 10^{L_{\text{dB}}^{(\text{env})}/10}$. Our measurement campaign has shown that the propagation channel can be accurately characterized as a narrowband Rayleigh block fading. Therefore, the instantaneous received power $\mathbf{P}_{\text{env}}$ has the following exponential distribution [60]:

$$f_{\mathbf{P}_{\text{env}}}(x) = \frac{1}{P_{\text{env}}} \exp\left\{ -\frac{x}{P_{\text{env}}} \right\}. \tag{7.8}$$

7.3 Link–Layer Performance

Transmission on a single link of interest strongly depends on the characteristics of the propagation channel and more precisely on its statistical variability, but also on the interference generated by the other surrounding nodes. More specifically, the traffic generated by a single sensing node will be analyzed under the well accepted slotted ALOHA system model. In this model, the nodes are supposed to transmit at discrete moments in time (called time slots) and the probability that a specific sensor has data to send is constant and will be noted as q. The node probability of transmission is a generic value in our analysis but it obviously depends on the medical application considered and can be precisely evaluated for any scenario, as it will be shown later.

We now provide the reader with the closed-form expressions of the link probability of success for a given node in the context of multiuser BANs.

7.3.1 Link Probability of Transmission in Multisensor Communications

The combination of the two propagation mechanisms presented in Subsections 7.2.1 and 7.2.2 allows us to derive a unified propagation model for a generic BAN. It can be observed that the degree of importance of each mechanism depends on the distance between transmitter and receiver. More precisely, in proximity, the dominant propagation mechanism is the on-body propagation described in Subsection 7.2.1. Above the crossover distance $d_{\text{cross}} \approx 25$ cm, the contribution of the environment becomes dominant and the second propagation mechanism, presented in Subsection 7.2.2, is the only relevant one. Therefore, a unified propagation model can be characterized as follows:

- In an outdoor environment, the average received power can be computed using Equation 7.4 (i.e., $\mathbb{E}[\mathbf{P}(d)] \propto P10^{\gamma d}$) and the instantaneous received power is determined by the log-normal fading channel model given by Equation 7.5.
- In an indoor environment:
  - If $d \leq d_{\text{cross}}$, the average received power can be computed using Equation 7.4 (i.e., $\mathbb{E}[\mathbf{P}(d)] \propto P10^{\gamma d}$) and the log-normal fading in Equation 7.5 is used.
  - If d > dcross, the average received power is approximately constant (i.e., $\mathbb{E}[\mathbf{P}(d)] = PL^{(\text{env})}$) and the instantaneous received power, owing to a Rayleigh faded channel model, has the distribution given by Equation 7.8.

In a BAN, all sensors need to transmit to a central controller and, in this sense, the scenario at hand can be interpreted as a multiuser scenario. Transmission over a link of interest is denoted with the subscript "0." Besides the intended transmitter, other nodes may be interfering. Depending on their distance to the receiver, the interfering nodes will be denoted differently. More precisely:

- In an indoor scenario, the interferers located at distances shorter than d_{cross} are referred to as "close-range interferers," their number is indicated as N_{close}, and the generic node will be denoted with a subscript $i \in \mathcal{N}_{\text{close}} \triangleq \{1,2,\ldots,N_{\text{close}}\}$.
- In an indoor scenario, the interferers located at distances longer than d_{cross} are referred to as "far-range interferers," their number is indicated as N_{far}, and the generic node will be denoted with a subscript $j \in \mathcal{N}_{\text{far}} \triangleq \{1,2,\ldots,N_{\text{far}}\}$.
- In an outdoor scenario, the number of interferers is indicated as N_{out}, and the generic node will be denoted with a subscript $k \in \mathcal{N}_{\text{out}} \triangleq \{1,2,\ldots,N_{\text{out}}\}$.

The transmission state of a node at time t is characterized by the following indicator variable:

$$\Lambda(t) = \begin{cases} 1 & \text{if the node is transmitting at time } t \\ 0 & \text{if the node is silent at time } t. \end{cases}$$

Assuming slotted transmissions (i.e., t can assume multiples of the slot time), a simple random access scheme is such that, at each time slot, a node transmits with probability q [61, p. 278]. Therefore, $\{\Lambda_i(t)\}_{t=1}^{\infty}, i \in \mathcal{N}_{\text{close}}$, $\{\Lambda_j(t)\}_{t=1}^{\infty}, j \in \mathcal{N}_{\text{far}}$, and $\{\Lambda_k(t)\}_{t=1}^{\infty}, k \in \mathcal{N}_{\text{out}}$ are sequences of Bernoulli RVs with $\mathbb{P}\{\Lambda_i(t)=1\} = \mathbb{P}\{\Lambda_j(t)=1\} = q, \forall t,i,j,k$.

A transmission in a given link is successful if and only if the signal-to-noise and interference ratio (SINR) at the receiver is above a certain threshold θ. This threshold value depends on the

receiver characteristics, the modulation format, and the coding scheme, among other aspects. The SINR at the receiving node of the link is given by

$$\text{SINR} \triangleq \frac{P_0(d_0)}{\text{N}_0\text{B}+P_{\text{int}}} \tag{7.9}$$

where $P_0(d_0)$ is the received power from the link source located at distance d_0, N_0 is the power noise spectral density, B the channel bandwidth, and P_{int} is the total interference power at the link receiver, that is, the sum of the instantaneous received powers from all the undesired transmitters. More precisely, in an indoor environment, one has:

$$P_{\text{int}}^{(\text{indoor})} \triangleq \sum_{i=1}^{N_{\text{close}}} \Lambda_i P_i(d_i) + \sum_{j=1}^{N_{\text{far}}} \Lambda_j P_{\text{env}} \tag{7.10}$$

and, in an outdoor environment, one has:

$$P_{\text{int}}^{(\text{outdoor})} \triangleq \sum_{k=1}^{N_{\text{out}}} \Lambda_k P_k(d_k). \tag{7.11}$$

Finally, as typical in the context of BANs, we assume that all nodes use the same transmit power, that is, $P_i(0) = P_j(0) = P_k(0) = P_0(0)$, $\forall i, j, k$.

7.3.1.1 Link Probability of Success with Short-Range Transmission in Indoor Scenarios

The link probability of success for a required threshold SINR value θ in the context of a short, indoor, log-normal faded link is equal to

$$\begin{aligned}
\mathcal{P}_{\text{close}}^{(\text{indoor})} &= \mathbb{P}\{\text{SINR} > \theta\} \\
&= \mathbb{E}_{\mathbf{P}_{\text{int}}}\left[\mathbb{P}\left\{\frac{P_0 L(d_0) X_0}{N_0 B + P_{\text{int}}} > \theta \middle| P_{\text{int}}^{(\text{indoor})}\right\}\right] \\
&= \mathbb{E}_{X,\Lambda,P_{\text{env}}}\left[1 - \mathbb{P}\left\{X_0 \le \theta \frac{N_0 B + P_{\text{int}}^{(\text{indoor})}}{P_0 L(d_0)}\right\}\right] \\
&= \mathbb{E}_{X,\Lambda,P_{\text{env}}}\left[\frac{1}{2} + \frac{1}{2}\,\text{erf}\left(\frac{-10}{\sigma\sqrt{2}} \log_{10}\left(\theta \frac{N_0 B + P_{\text{int}}^{(\text{indoor})}}{P_0 L(d_0)}\right)\right)\right].
\end{aligned} \tag{7.12}$$

In Appendix A at the end of this chapter, it is shown that

$$\zeta(z;\sigma) \triangleq \frac{1}{2} + \frac{1}{2}\,\text{erf}\left(\frac{-10\log_{10} z}{\sigma\sqrt{2}}\right) \approx \sum_{m}^{n} c_m \exp(-a_m z)$$

where $\{c_m\}_{m=1}^{n}$ and $\{a_m\}_{m=1}^{n}$, where n is an integer determined by the expansion accuracy and is a suitable coefficient. By using the function $\zeta(\cdot;\cdot)$ and recalling Expression 7.10 for the interference power, the link probability of success (Equation 7.12) can be written as follows:

$$\begin{aligned}\mathcal{P}_{\text{close}}^{(\text{indoor})} &= \mathbb{E}\left[\zeta\left(\theta\frac{\mathbf{P}_{\text{int}}^{(\text{indoor})}}{P_0 L(d_0)};\sigma\right)\right] \\ &= \sum_{m=1}^{n} c_m \exp\left(\frac{-a_m\theta N_0 B}{P_0 L(d_0)}\right)\times\mathbb{E}\left[\exp\left(-a_m\theta\sum_{i=1}^{N_{\text{close}}}\frac{L(d_i)}{L(d_0)}\mathbf{X}_i\Lambda_i\right)\right]\times\mathbb{E}\left[\exp\left(-a_m\theta\sum_{j=1}^{N_{\text{far}}}\frac{\mathbf{P}_{\text{env}}}{P_0 L(d_0)}\Lambda_j\right)\right]\end{aligned} \tag{7.13}$$

where, in the last passage, we have used the fact that the RVs $\{\mathbf{\Lambda}_i, \mathbf{\Lambda}_j, P_{\text{env}}, \text{and } X_i\}$ are independent. The middle term in the second line of the right-hand side of Equation 7.13 can be further expressed as

$$\begin{aligned}\mathbb{E}\left[\exp\left(-a_m\theta\sum_{i=1}^{N_{\text{close}}}\frac{L(d_i)}{L(d_0)}\mathbf{X}_i\Lambda_i\right)\right] &= \prod_{i=1}^{N_{\text{close}}}\mathbb{E}\left[\exp\left(-a_m\theta\frac{L(d_i)}{L(d_0)}\mathbf{X}_i\Lambda_i\right)\right] \\ &= \prod_{i=1}^{N_{\text{close}}}\left\{\mathbb{P}\{\Lambda_i=0\}\times 1+\mathbb{P}\{\Lambda_i=1\}\times\mathbb{E}\left[\exp\left(-a_m\theta\frac{L(d_i)}{L(d_0)}\mathbf{X}_i\right)\right]\right\} \\ &= \prod_{i=1}^{N_{\text{close}}} q\int_0^{\infty}\exp(-a_m\theta 10^{\gamma(d_i-d_0)}x)f_{\mathbf{X}}(x)\mathrm{d}x+(1-q).\end{aligned} \tag{7.14}$$

The final integral expression in Equation 7.14 can be numerically computed. The term in the third line of the expression in Equation 7.13 can be expressed as follows:

$$\begin{aligned}\mathbb{E}\left[\exp\left(-a_m\theta\sum_{j=1}^{N_{\text{far}}}\frac{\mathbf{P}_{\text{env}}}{P_0 L(d_0)}\Lambda_j\right)\right] &= \prod_{j=1}^{N_{\text{far}}}\mathbb{E}\left[\exp\left(-a_m\theta\frac{\mathbf{P}_{\text{env}}}{P_0 L(d_0)}\Lambda_j\right)\right] \\ &= \prod_{j=1}^{N_{\text{far}}}\left\{\mathbb{P}\{\Lambda_j=0\}\times 1+\mathbb{P}\{\Lambda_j=1\}\times\mathbb{E}\left[\exp\left(-a_m\theta\frac{\mathbf{P}_{\text{env}}}{P_0 L(d_0)}\right)\right]\right\} \\ &= \left[(1-q)+q\int_0^{\infty}\exp\left(-a_m\theta\frac{x}{P_0 L(d_0)}\right)\frac{1}{P_{\text{env}}}e^{-x/P_{\text{env}}}\,\mathrm{d}x\right]^{N_{\text{far}}} \\ &= \left[1-\frac{\theta q}{\frac{L_0 10^{\gamma d_0}}{L^{(\text{env})}}+\theta}\right]^{N_{\text{far}}}.\end{aligned} \tag{7.15}$$

Finally, by using Equations 7.14 and 7.15 into Equation 7.13, the link probability of success can be given by the expression in Equation 7.16.

$$\mathcal{P}_{\text{close}}^{(\text{indoor})} = \sum_{m=1}^{n} c_m \underbrace{\exp\left(\frac{-a_m \theta N_0 B}{P_0 L_0 10^{\gamma d_0}}\right)}_{\text{Background noise}} \times \prod_{i=1}^{N_{\text{close}}} \underbrace{\left[q \int_0^{\infty} \exp(-a_m \theta 10^{\gamma(d_i - d_0)} x) f_{\mathbf{X}}(x) \mathrm{d}x + (1-q) \right]}_{\text{Close-range interferers}} \times \underbrace{\left[1 - \frac{\theta q}{\frac{L_0 10^{\gamma d_0}}{L^{(\text{env})}} + \theta} \right]^{N_{\text{far}}}}_{\text{Far-range interferers}} \tag{7.16}$$

7.3.1.2 Link Probability of Success with Long-Range Transmission in Indoor Scenarios

The Rayleigh-faded channel model applies to indoor links with length $d > d_{\text{cross}}$. In this scenario, $\mathbb{E}[\mathbf{P}(d)] \approx P_{\text{env}}$ (for both the intended transmitter and interferers) and the link probability of success can be expressed as follows:

$$\begin{aligned}
\mathcal{P}_{\text{far}}^{(\text{indoor})} &= \mathbb{P}\{SINR > \theta\} \\
&= \mathbb{E}_{\mathbf{P}_{\text{int}}}\left[\mathbb{P}\{SINR > \theta\} \mid \mathbf{P}_{\text{int}}^{(\text{indoor})} \right] \\
&= \mathbb{E}\left[\exp\left\{ -\frac{\theta(N_0 B + \mathbf{P}_{\text{int}}^{(\text{indoor})})}{P_{\text{env}}} \right\} \right] \\
&= \exp\left(\frac{-\theta N_0 B}{P_{\text{env}}}\right) \times \mathbb{E}\left[\exp\left(-\theta \sum_{i=1}^{N_{\text{close}}} \frac{P_i L(d_i)}{P_{\text{env}}} \mathbf{X}_i \Lambda_i \right) \right] \times \mathbb{E}\left[\exp\left(-\theta \sum_{j=1}^{N_{\text{far}}} \frac{\mathbf{P}_{\text{env}}}{P_{\text{env}}} \Lambda_i \right) \right].
\end{aligned} \tag{7.17}$$

It can be observed that the terms in the second and third lines at the right-hand side of Equation 7.17 are similar to Equations 7.14 and 7.15. Therefore, by using the same derivation of Subsection 7.3.1.1, with $P_0 L(d_0)$ replaced by $P_0 L^{(\text{env})}$, one has

$$\mathbb{E}\left[\exp\left(-\theta \sum_{i=1}^{N_{\text{close}}} \frac{P_i L(d_i)}{P_{\text{env}}} \mathbf{X}_i \Lambda_i \right) \right] = \prod_{i=1}^{N_{\text{close}}} \left[q \int_0^{\infty} \exp\left(-\theta \frac{L_0 10^{\gamma d_i}}{L^{(\text{env})}} x \right) f_{\mathbf{X}}(x) \mathrm{d}x + (1-q) \right] \tag{7.18}$$

and

$$\mathbb{E}\left[\exp\left(-\theta \sum_{j=1}^{N_{\text{far}}} \frac{\mathbf{P}_{\text{env}}}{P_{\text{env}}} \Lambda_i \right) \right] = \left[1 - \frac{\theta q}{1+\theta} \right]^{N_{\text{far}}}. \tag{7.19}$$

By inserting Equations 7.18 and 7.19 into Equation 7.17, one obtains the final expression (Equation 7.20) for the probability of successful transmission on the link.

$$\mathcal{P}_{\text{far}}^{(\text{indoor})} = \underbrace{\exp\left(\frac{-\theta N_0 B}{P_{\text{env}}}\right)}_{\text{Background noise}} \times \prod_{i=1}^{N_{\text{close}}} \underbrace{\left[q \int_0^{\infty} \exp\left(-\theta \frac{L_0 10^{\gamma d_i}}{L^{(\text{env})}} x \right) f_{\mathbf{X}}(x) \mathrm{d}x + (1-q) \right]}_{\text{Close-range interferers}} \times \underbrace{\left[1 - \frac{\theta q}{1+\theta} \right]^{N_{\text{far}}}}_{\text{Far-range interferers}} \tag{7.20}$$

7.3.1.3 Link Probability of Success in Outdoor Scenarios

In these scenarios, the links are subject to log-normal fading and exponential power decreases. The link probability of success can simply be derived by using the derivation in Subsection 7.3.1.1, setting $N_{\text{out}} = N_{\text{close}}$ and $N_{\text{far}} = 0$ (this does not mean that there are not far interferers, but that their propagation model is simply the same of close interferers). Therefore, the computation of the link probability of success $\mathcal{P}^{(\text{outdoor})}$ is straightforward from Equation 7.16, and the final expression is given in Equation 7.21.

$$\mathcal{P}^{(\text{outdoor})} = \sum_{m=1}^{n} c_m \underbrace{\exp\left(\frac{-a_m \theta N_0 B}{P_0 L_0 10^{\gamma d_0}}\right)}_{\text{Background noise}} \times \prod_{i=1}^{N_{\text{out}}} \left[q \int_0^{\infty} \exp(-a_m \theta 10^{\gamma(d_i - d_0)} x) f_{\mathbf{X}}(x) \mathrm{d}x + (1-q) \right] \tag{7.21}$$

7.3.2 Energy Consumption and Minimum Transmit Power

From the above relations, the minimum transmission power on a link can be easily derived. It is defined as the power required to achieve a threshold link probability of success $\mathcal{P}_{\text{th}}$ in a noise-limited regime, that is, when all other nodes are silent. Therefore, by recalling Equations 7.16, 7.20, and 7.21 and setting $N_{\text{out,close,far}} = 0$, one has:

$$P_0^{(\text{indoor})} \geq \begin{cases} \dfrac{\theta k_{\text{b}} T B}{L_0 10^{\gamma d_0} \zeta^{-1}(\mathcal{P}_{\text{th}})} & \text{if } d < d_{\text{cross}} \\ -\dfrac{\theta k_{\text{b}} T B}{\ln \mathcal{P}_{\text{th}}} & \text{if } d \geq d_{\text{cross}} \end{cases} \tag{7.22}$$

where N_0 has been expressed as Tk_{b}, with T being the room temperature (dimension, K) and $k_{\text{b}} = 1.38 \times 10^{-23}$ J/K being Boltzmann's constant, and B is the transmission bandwidth. For the outdoor scenario, one obtains:

$$P_0^{(\text{outdoor})} \geq \frac{\theta k_{\text{b}} T B}{L_0 10^{\gamma d_0} \zeta^{-1}(\mathcal{P}_{\text{th}})}. \tag{7.23}$$

where $\mathcal{P}_{th}$ is the threshold link probability of success. In Figure 7.5, the minimum transmission power is presented as a function of the transmission distance d_0 and the threshold link probability of success $\mathcal{P}_{th}$. It can be observed from Figure 7.5a that, in an indoor scenario, there are reflections off the walls.

Finally, note that in the following, we will consider only interference-limited networks, that is, scenarios in which the conditions in Equations 7.22 or 7.23 are satisfied. Formally, this situation is equivalent to letting the thermal noise $N_0B = 0$ in Equation 7.9.

7.4 Link-Level Throughput and Delay

In this article, we consider multiuser communications in which a transmission will be defined as successful if and only if the associated transmission link is not in an outage. This corresponds to requiring that the (instantaneous) SINR of the link is above the threshold θ, that is,

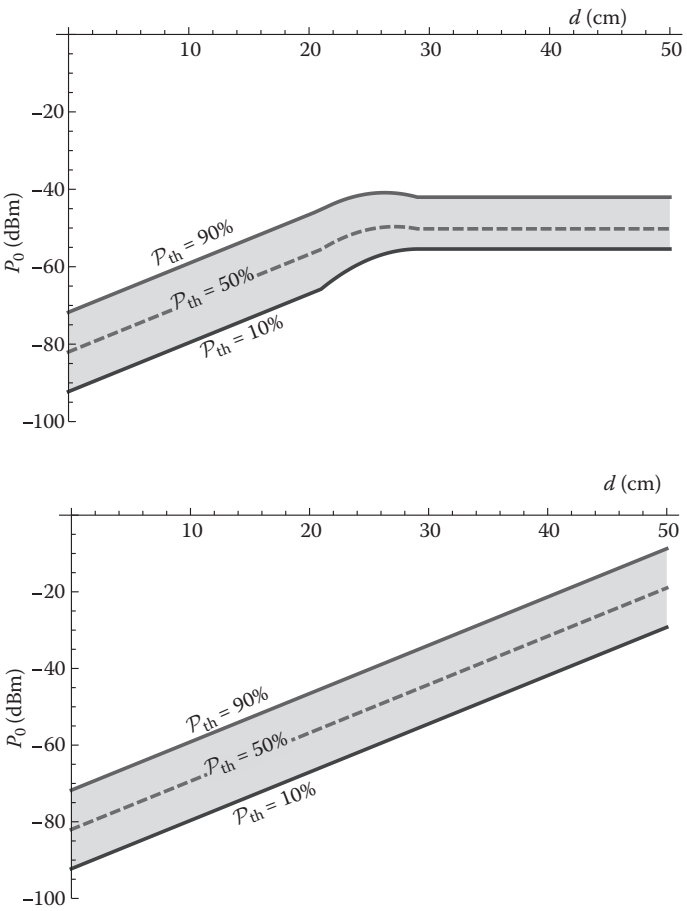

Figure 7.5 Minimum transmission power for a given link probability of success and as a function of the distance.

$$\mathcal{P}^{(\text{link})} = \mathbb{P}\{\text{SINR} > \theta\}. \tag{7.24}$$

Obviously, this probability depends on the physical channel characteristics, the shadowing on the links, the mobility of the nodes (e.g., if the node is located on an arm), and the modulation in use. For instance, in a ZigBee system or, in general, with low-throughput BANs, a value of $\theta = 5$ dB is sufficient. In the article, we refer to the IEEE 802.15.6 standard, which allows the use of two access control schemes: (i) a random, slotted ALOHA access and (ii) a deterministic TDMA access.

In a slotted ALOHA system, the time is divided in equal, discrete elements called *time slots*. During each time slot, a node has a fixed probability of transmitting a packet. In the remainder of this article, this value is noted q (nondimensional). During this time slot, any number of nodes can attempt a transmission and collisions may occur. As a consequence, the delay in a slotted ALOHA system is directly linked to the number of (re)transmissions needed to send (or forward) a packet, which in turn is directly proportional to the link probability of success and the overall activity of the network (through the value of q).

On the other hand, in a TDMA system, the time is exactly divided in a fixed number of slots. Each slot is then allocated to a given a node and it is allowed to transmit only during its time slot. At any other time, the node must remain silent. Therefore, the delay depends on the (deterministic) amount of time to wait before a dedicated slot takes place. In a generic approach, it can be supposed that a relay node will allocate exactly one slot per sensor to receive its data and a slot per sensor for the forwarding uplink. This in turn depends on the routing tree and the quality of service (QoS) requirements.

Finally, we define a probabilistic throughput value as the average probability of successful transmission $\mathcal{P}^{(\text{link})}$ multiplied by the probability that the transmitter actually has a packet to transmit q, that is,

$$\tau \triangleq q\mathcal{P}^{(\text{link})}. \tag{7.25}$$

Obviously, in the slotted ALOHA scheme, the value of $\mathcal{P}^{(\text{link})}$ can be $\mathcal{P}^{(\text{indoor})}_{\text{close}}$, $\mathcal{P}^{(\text{indoor})}_{\text{far}}$, or even $\mathcal{P}^{(\text{outdoor})}$, depending on the scenario and the link of interest. On the other hand, in the TDMA scheme, it is the average activity period, that is, the amount of time that a node is actually allowed to transmit in the time division scheme. We now provide the reader with the exact computation of the delay and the corresponding throughput.

7.4.1 Random Access BANs

The slotted ALOHA multiple access scheme [19] was recently proposed by the IEEE 802.15.6 working group as one of the reference medium access control (MAC) schemes for wireless body networks in the context of narrow-band communications [20]. An example of slotted ALOHA is given in Figure 7.6. In particular, in each time slot, the nodes are assumed to transmit independently with a certain fixed probability [21]. This approach is supported by the observations in studies by Huhta and Webster [22, p. 278], Wood and Ewins [21], and Webster [23], in which it is shown that the traffic generated by nodes using a slotted random access MAC protocol can be modeled with a Bernoulli distribution. In fact, in more sophisticated MAC schemes, the probability of transmission at a node can be modeled as a function of general parameters, such as queuing statistics, the queue-dropping rate, the channel outage probability incurred by fading [24], the adaptation of the sampling rate to the patient's condition [25], the MAC strategy used [26], and

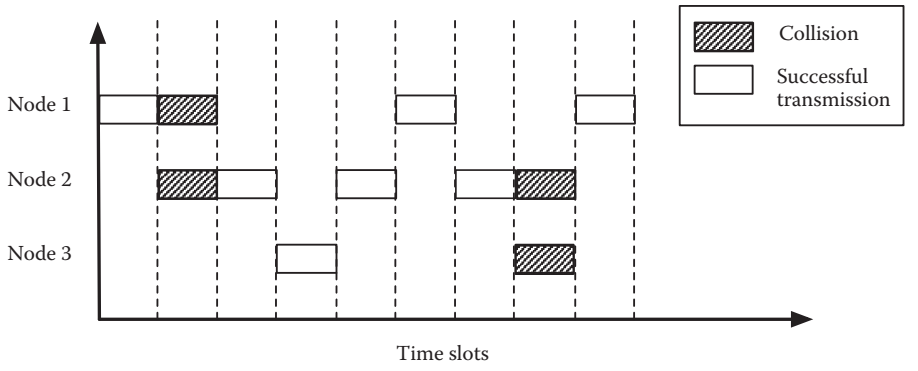

Figure 7.6 Slotted ALOHA scheme.

others. Because the effects of these parameters are not the focus of this study, the interested reader is referred to the existing literature [27–29] for further details.

In a slotted ALOHA system, the delay is directly connected to the number of (re)transmissions needed to send or forward a packet, which depends on the number of nodes and especially their probability of transmission. More precisely, the average number of transmissions can be written as:

$$E[r] = \sum_{r=1}^{\infty} rQ_r$$

where Q_r is the probability if a successful communication takes place exactly at the rth attempt (i.e., $r - 1$ unsuccessful transmissions and a successful transmission). It is expressed as:

$$Q_r = (1 - P_s)^{r-1} P_s$$

where P_s denotes the link probability of success. It can be observed that the variable r is a geometric random variable with parameter P_s. Therefore, the average delay in slotted ALOHA scheme, in terms of time slots, is exactly:

$$D_{\text{ALOHA}} = E[r] = \frac{1}{P_s}. \tag{7.26}$$

By recalling the definition of the link throughput given in Equation 7.25 and using the relation in Equation 7.26, one finally obtains the link throughput

$$\tau_{\text{ALOHA}} = qP_s = \frac{q}{D_{\text{ALOHA}}} \tag{7.27}$$

which shows that the network throughput will directly depend on the value of q (through the value of P_s, which models the number of collisions on a given link).

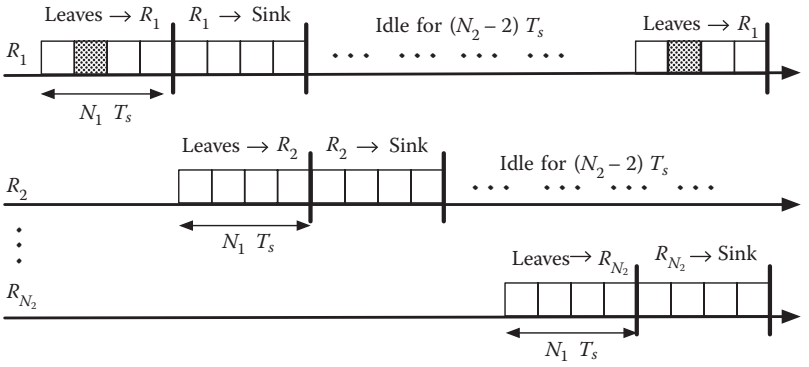

Figure 7.7 TDMA chronogram.

7.4.2 TDMA BANs

In a TDMA system, each node transmits during a dedicated time slot and, as consequence, in an interference-limited regime, one has $P_s = 1$. The delay D_{TDMA} only depends on the amount of time to wait before a dedicated slot takes place. In a generic approach, it can be supposed that a relay node will allocate exactly one slot per sensor to receive its data and a slot per sensor for the forwarding uplink. Note that this is an anticipation on the computation of the route delay. Indeed, on the opposite of the studied random access scheme (i.e., slotted ALOHA), the exact computation of the link delay in TDMA requires that the effect of relaying be taken into account, which in turn depends on the topology of the routes.

In Figure 7.7, the slot allocations (i.e., chronogram) are presented for each relay (noted as $R_1, R_2, \ldots, R_{N_2}$). The time slots have a fixed duration of T_s (dimension, s). As can be seen from Figure 7.7, each relay needs a frame of N_1 time slots to collect the packets (possibly generated) from its N_1 leaves. It then waits another frame (N_1 time slots) to forward them to the sink. At this point, it needs to remain idle for $(N_2 - 2)$ frames, as the sink is busy collecting the packets from the other relays. This corresponds to assuming the same transmission rates at leaves and relays, and the same TDMA-based approach at first and second layers. Therefore, the distance between two consecutive slots assigned to a given leaf is equal to $N_1 \cdot N_2$ slots: when a leaf generates a packet, it needs to wait a number of slots between 0 (its slot is the current one) and $N_1 \cdot N_2 - 1$ (its slot just passed).* As each number of slots has the same probability, the average delay (expressed in time slots) experienced by a given leaf node is

$$D_{\text{TDMA}} = \frac{1}{N_2 \cdot N_1 - 1} \sum_{i=0}^{N_2 \cdot N_1 - 1} i = \frac{N_2 \cdot N_1}{2}. \tag{7.28}$$

The above derivation for D_{TDMA} represents an "average" scenario in which a node generates at most a packet in an interval equal to $N_1 \cdot N_2$ time slots. If, on the other hand, more than one

* We assume that packet generation is at the beginning of a slot.

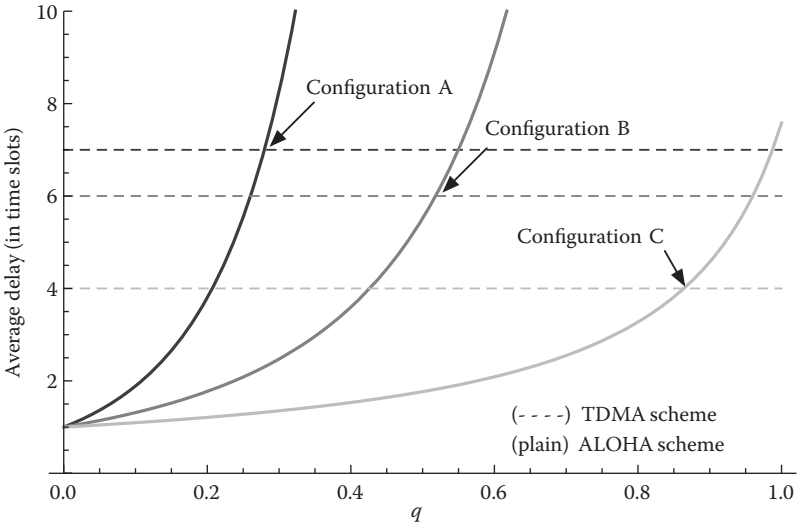

Figure 7.8 Qualitative description of the average delay at the relay nodes for TDMA and slotted ALOHA schemes as functions of sensor probability of transmission q and for various network topologies.

packet is generated during a time slot, it means that as soon as a leaf has transmitted a packet to its relay, it is likely to soon generate a new packet, which will wait a period longer than that of Equation 7.28. This waiting period is at most $N_1 \cdot N_2$ time slots. Therefore, in general, it can be stated that

$$\frac{N_2 \cdot N_1}{2} \leq D_{\text{TDMA}} \leq N_2 \cdot N_1.$$

In Figure 7.8, the average delay (expressed in contention time slots) incurred by a leaf to reach its relay is shown in a qualitative manner and as a function of the transmission probability q. Note that in the TDMA case, the expression does not depend on q, because in TDMA systems, a leaf needs to wait for its assigned time slot. Finally, one can anticipate that, as it will be formally demonstrated later, when the node probability of transmission is low, the slotted ALOHA significantly outperforms the TDMA scheme. However, for increasing probability of transmission, that is, for increasing traffic load, there exists a critical threshold above which the TDMA scheme is to be preferred.

7.5 Reliable Routing and Optimal Topology in Multihop BAN

Assuming that all links of a route are independent and that a packet erroneously transmitted on any link of a route is not retransmitted, the route probability of success can be expressed as

$$\mathcal{P}^{(\text{route})} = \prod_{i}^{n_{\text{hops}}} \mathcal{P}_i^{(\text{link})} \tag{7.29}$$

where $\mathcal{P}_i^{(\text{link})}$ is the link probability of success on the ith link of the route and n_{hops} is the route length. In this sense, the derived expression (Equation 7.29) will be an upper bound for successful transmission probability, which corresponds to a real-time streaming of data based on a datagram-oriented transport. More precisely, the connectionless transmission modes [e.g., user datagram protocol (UDP) and real-time streaming protocol (RTSP)] are stateless by nature and allow the nonblocking sending of data stream, which is a requirement in medical applications but, as a consequence, this transport mode does not allow for successful transmission monitoring and resending of nonreceived packets.

QoS in BANs is a nontrivial and relevant question in this very specific context. In a general manner, QoS comprises the requirements on all aspects of a data stream connection, such as the maximum acceptable loss, delay, variability of the service, etc. In the absence of QoS, the delivery network may suffer from dropped packets, excessive latency, jitter, and out-to-order delivery. In the field of medical applications, guaranteed packet delivery is the most important requirement and other issues (such as delay or jitter) can be considered of less importance. First, as discussed previously, medical sensing is more likely to use connectionless transmission modes, such as real-time protocol (RTP; RFC 3350), to ensure a fluid delivery of data packets. The RTP protocols ensure that out-of-order packets are correctly delivered by tagging the packet sequence using an increasing 16-bit sequence number. Second, due to the limited size of the network, jitter (the variability of the data delivery delay) can be fairly neglected because no end-to-end retransmission can take place. Also, once established, the routing tree will be stable for the entire monitoring session, which further guarantees limited jitter. Finally, the existence of a constant delay is not important in a pure monitoring system, that is, a system that performs the collection of vitals without feedback actions. However, as it will be presented later, in a random access network, delay can grow exponentially and even become unbounded. This is not the case in a deterministic, TDMA network. Therefore, specific attention will be paid to the computation of the delay and the comparison of both access methods.

To summarize, the QoS in a medical application can be formulated as the requirement that (i) the number of losses is small and (ii) the delay is noninfinite. To translate these two requirements into equations, we propose the following framework for the computation of the optimal routing tree. On the basis of the expression in Equation 7.29, we define that a route has an acceptable QoS if and only if a minimum end-to-end transmission rate can be achieved, that is,

$$\begin{cases} D^{(\text{route})} < \infty \\ \mathcal{P}^{(\text{route})} \geq \mathcal{P}_{\text{min}}^{(\text{medical})} \end{cases} \tag{7.30}$$

where $D^{(\text{route})}$ is the end-to-end route delay and the value $\mathcal{P}_{\text{min}}^{(\text{medical})}$ depends on the medical application of interest and is defined by the practicians. It is usually high, that is, $\mathcal{P}_{\text{min}}^{(\text{medical})} > 90\%$ is a reasonable expectation.

7.5.1 Routing in BAN Networks

Routing is the process of selecting the optimal path (with respect to an objective function to be maximized or minimized) in a network along which data traffic flows. In the context of a medical monitoring scenario, routing is intended to find the optimal way to send information through the network, from sensors to the sink, under the minimum QoS requirements expressed in Equation 7.30.

In a study by Dricot et al. [62], a preliminary performance analysis of BANs with star topologies was carried out. Indeed, these topologies are simple to implement but not well-suited for medical applications because they exhibit a significant power consumption [63] and cannot perform in-network data aggregation [64,65].

In Figure 7.9, an illustrative medical application is presented. The corresponding routing scheme (plain bold lines) is derived from the connectivity graph (dashed lines). The specific routes are chosen so that the QoS meets the medical requirements. As shown in Figure 7.9, wireless transmissions allow multiple possible paths for the routing of packets from the sensing nodes to the collecting sink. Furthermore, due to the short distance nature of BAN communications, direct transmissions are feasible almost all of the time but they are subject to more interference. Therefore, the objective of the routing algorithm is to determine the most reliable routes, in terms

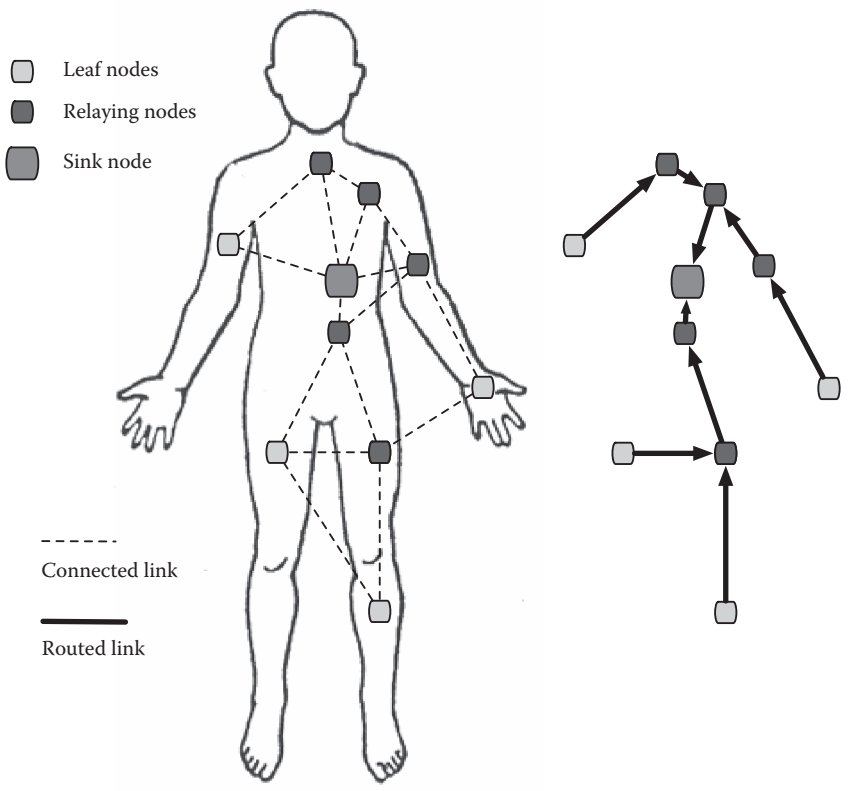

Figure 7.9 Medical application of body sensor networks. Possible links are presented in dashed lines and the routing tree wrt. to QoS requirements is drawn in bold lines.

of the number of hops and relaying nodes, to transport an information stream from a leaf node to the sink. Also, due to the dynamic nature of the network configuration (e.g., arms moving, switching from indoors to outdoors, and others), a dynamic routing algorithm is mandatory, that is, routes cannot be determined a priori for any medical application and forced into the nodes.

Dynamic routing protocols are based on well-known routing tree exploration techniques. These protocols can be divided into two major techniques: link-state and distance-vector. The latter class of protocols was designed for very large architectures, such as the Internet, and is based on a decentralized, step-by-step convergence approach. This class of protocols has less computational complexity but will not be considered here because it exhibits certain limitations that must be avoided in medical applications. These include the well-known count-to-infinity problem (i.e., routing loops) and slow convergence times (due to the iterative nature of the algorithm).

On the other hand, link-state algorithms are performed by each node in the network, that is, every node constructs a map of the connectivity to the network and then independently calculates the best logical path to every possible destination in the network. Practically, the routing task can also be implemented in a centralized node (e.g., the sink node) and the routing tables are subsequently redistributed to the sensing nodes. The incurred overhead of control messages (signaling traffic) is negligible with respect to the data streams' load. Modern link-state algorithms are usually based on variants of the Dijkstra algorithm.

7.5.2 Link-State Routing: Dijkstra's Algorithm

Dijkstra's algorithm [66] is a graph search algorithm that solves the single-source shortest path problem for a graph with nonnegative edge path costs producing the shortest path tree. More precisely, for a given source vertex (node) in the graph, the algorithm computes the path with the lowest cost (i.e., the shortest path with respect to a cumulative cost metric) between that vertex and every other vertex. It can also be used for finding the cost of the shortest path from a given vertex to a specific destination vertex by stopping the algorithm once the shortest path to the destination vertex has been determined. For instance, if the vertices of the graph represent the network connectivity and edge path costs represent the link probability of errors between pairs of nodes connected, Dijkstra's algorithm can be used to find the route with the highest probability of success. This route is denoted as the "optimal route," with respect to a cost function or the "shortest path." Because Dijkstra's algorithm is simple to implement, has a reduced complexity, and is proven to be extremely stable, it is widely used in network routing protocols, most notably in intermediate system–to–intermediate system (IS-IS; RFC 1142) and open shortest path first (OPSF; RFC 2328).

The algorithm works by using the following iterative steps:

1. Assign a tentative distance value to every node: set it to zero for the initial node and to infinity for all other nodes.
2. Mark all nodes unvisited. Set the initial node as current. Create a set of unvisited nodes called the unvisited set consisting of all the nodes except the initial node.
3. For the current node, consider all of its unvisited neighbors and calculate their tentative distances. For example, if the current node A is marked with a tentative distance of 6, and the edge connecting it with a neighbor B has length of 2, then the distance to B (through A) will be 6 + 2 = 8. If this distance is less than the previously recorded tentative distance of B, then overwrite that distance. Even though a neighbor has been examined, it is not marked as visited at this time, and it remains in the unvisited set.

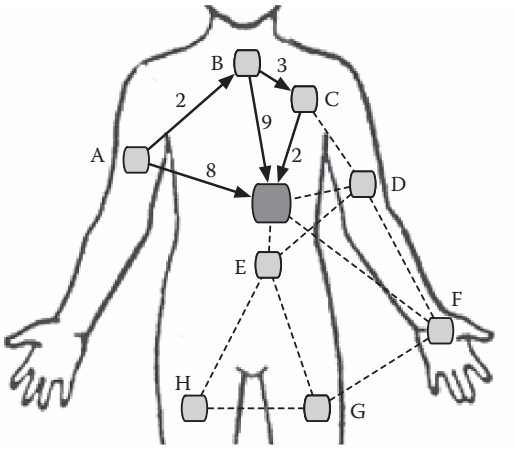

Figure 7.10 Scenario with multiple communication links between the nodes and the sink. On each link, the cost metric is presented.

4. When we are done considering all of the neighbors of the current node, mark the current node as visited and remove it from the unvisited set. A visited node will never be checked again; its distance recorded now is final and minimal.
5. If the destination node has been marked visited (when planning a route between two specific nodes) or if the smallest tentative distance among the nodes in the unvisited set is infinity (when planning a complete traversal), then stop. The algorithm has finished.
6. Set the unvisited node marked with the smallest tentative distance as the next "current node" and go back to step 3.

A pictorial example is presented in Figure 7.10, in which three possible paths connect the sensor node A to the sink node. As can be observed, several paths are possible and, mode specifically, the A sink has a cost of 8, the A-B sink has a cumulative cost of 2 + 9 = 11, and the A-B-C sink has a cost of 2 + 3 + 2 = 7. Therefore, the A-B-C sink is picked up because it is the lowest costing candidate.

7.5.3 Medical Nodes' Maximum Probability of Transmission

In this case, we consider a situation with a limited amount of sensors located on specific parts of the human body. Because the number of sensors in a real-life situation will range between 10 and 18, the density of the corresponding sensor network is low. Moreover, in most medical applications, not all sensors are used to monitor the patient's state, resulting in a sparse deployment that is specific to body sensor networks. For the purpose of this analysis, a particular distribution of nodes has been chosen and is represented in Figure 7.11. In the remainder of this performance analysis, the nodes are numbered as follows: 1, EEG; 2, EMG1; 3, EMG2; 4, EMG3; 5, ECG; 6, NFL; 7, VAB; 8, VTH; 9, PTL; and 10, SINK. The medical purposes of each sensor and its networking characteristics are introduced in Table 7.1.

In medical applications, the node probability of transmission is bound by two constraints: (1) the minimum sampling rate of the medical sensor (reported in Table 7.1) and (2) the minimum

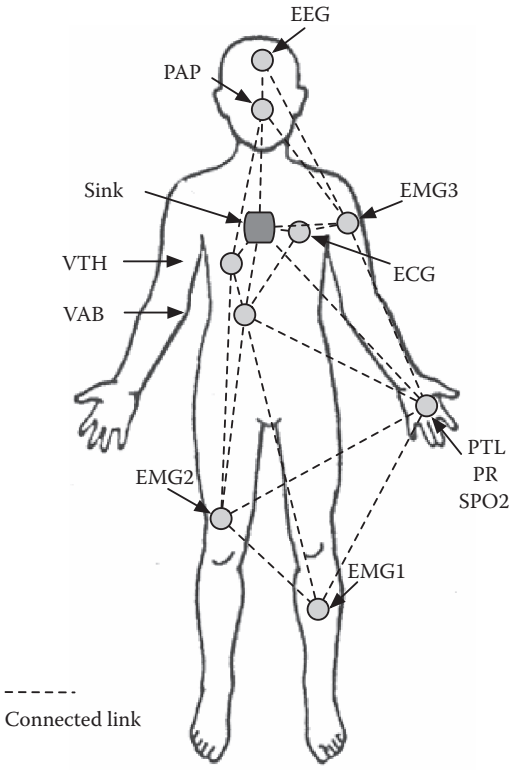

Figure 7.11 Medical scenario of interest for routing performance evaluation and its connectivity topology.

route probability of success, which translates into a maximum node transmission rate. Therefore, a computation of the maximum value for the transmission probability (noted as $q_{\max}$) is the first step before any analysis. The determination of this value is an iterative process, that is, for a given value of the route probability of success $\mathcal{P}_{\min}^{(\text{route})}$, the transmission rate of the nodes (through the quantity q) is increased at each iteration until $\mathcal{P}_{\min}^{(\text{route})}$ is reached. The corresponding value of the node probability of transmission is then reported as $q_{\max}$.

Note that, to further ensure the robustness of our analysis, the value of $\mathcal{P}_{\min}^{(\text{route})}$ is always calculated over the worst possible route. More precisely, all possible routing trees are computed and the value $\mathcal{P}_{\min}^{(\text{route})}$ corresponds to the lowest possible route probability of success observed on all possible network configurations. Figure 7.12 presents the medical nodes' maximum probability of transmission in a 10-node setup and as a function of the route minimum probability of success $\mathcal{P}_{\min}^{(\text{route})}$. It can be observed that the medical reporting rate decreases exponentially as the value of $\mathcal{P}_{\min}^{(\text{route})}$ increases. As a consequence, reducing the packet loss in the entire network is extremely difficult if the route quality is expected or required to be high. Furthermore, for values of $\mathcal{P}_{\min}^{(\text{route})} \geq 0.7$, which is in the functioning region of a real-life medical body sensor network, the value of $q_{\max}$ decreases linearly. In that region, the value of $q_{\max}$ less than or equal to 0.005, meaning that the random access strategy does work, but only if the medical reporting rate is low. In any other case (emergency increase of the sampling of the vitals, high density of nodes, high traffic sensors, etc.), the use of the TDMA strategy is mandatory.

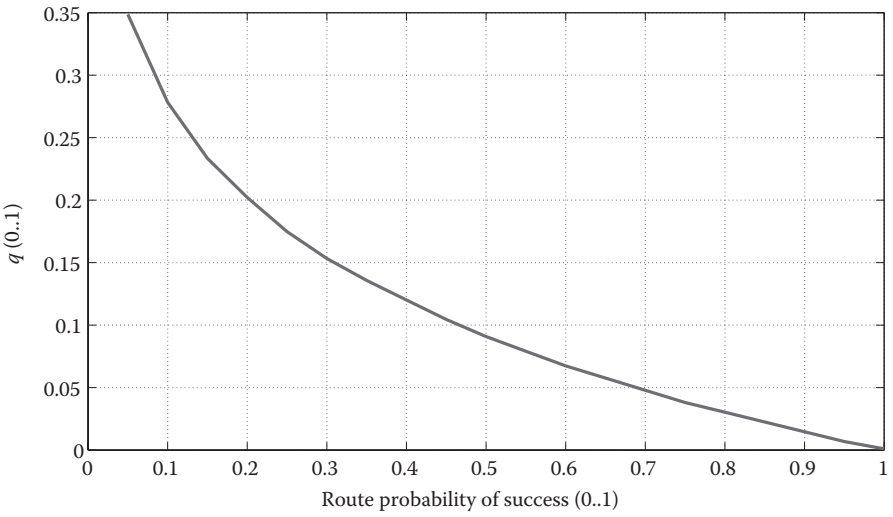

Figure 7.12 Probability of transmission versus minimum route probability of success in medical scenario.

Finally, the simulations were conducted for uplink and downlink traffic. In Figure 7.13, the medical nodes' maximum probability of transmission is reported as a function of the minimum route probability of success for the two traffic modes and in the case of the random access network. It can be observed that the difference is neglectable, and the prior analysis holds both in the uplink and the downlink communications.

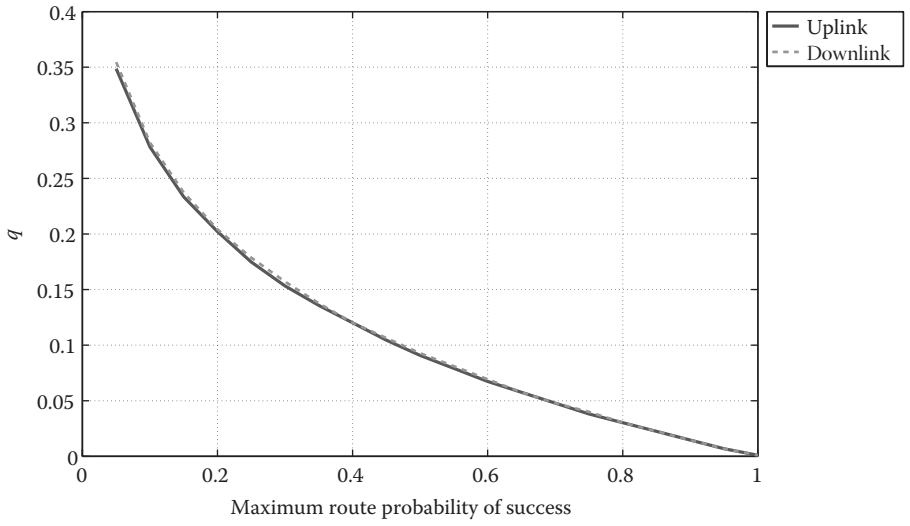

Figure 7.13 Uplink and downlink performance in medical scenario.

7.5.4 Optimum Routing Tree Computation and Corresponding Route Performance

When the computation of the maximum suitable value of $q_{\max}$ is completed, the next step is to derive the optimum routing tree of the random access network. The optimal routing tree is a collection of all the best paths between the central node (i.e., the sink node) and all the other medical sensor nodes, printed in the form of a tree graph in which the sink node is the root and sensors are the leaves.

The computation of the best path to reach every single leaf node is done with the Dijkstra algorithm presented in Section 7.5.2. To properly run the Dijkstra algorithm, one needs to assign a weight value on each link of the network such that a high link probability of success translates into a low link weight. Starting from the link probability of success is not possible because the definition in Equation 7.29 yields

$$\begin{aligned} 1-\mathcal{P}^{(\text{route})} &= 1-\prod_{i}^{n_{\text{hops}}}\mathcal{P}_i^{(\text{link})} \\ &= 1-\left[(1-\mathcal{P}_2^{(\text{link})})(1-\mathcal{P}_1^{(\text{link})})\right] \end{aligned} \tag{7.31}$$

which cannot be used in Dijkstra's algorithm because it is not an additive function of the probability of success of each link. This problem can be solved by considering a logarithmic version of the link costs. More precisely, the objective of Dijkstra's algorithm is to maximize $\mathcal{P}^{(\text{route})}$, which can be seen as an equivalent to minimizing the quantity $1/\mathcal{P}^{(\text{route})}$. Furthermore, by recalling that the logarithm is a continuous, strictly increasing function of its argument, minimizing the quantity $\mathcal{P}^{(\text{route})}$ can be equivalently rewritten as minimizing the function $\log_{10}\mathcal{P}^{(\text{route})}$ and it can be written (in the case of a n-hops scenario) as:

$$\begin{aligned} \max\left\{\log_{10}\mathcal{P}^{(\text{route})}\right\} &\Leftrightarrow \min\left\{\log_{10}\frac{1}{\mathcal{P}^{(\text{route})}}\right\} \\ &\Leftrightarrow \min\left\{\log_{10}\frac{1}{\prod_{i}^{n_{\text{hops}}}\mathcal{P}_i^{(\text{link})}}\right\} \\ &\Leftrightarrow \min\left\{\sum_{i}^{n_{\text{hops}}}\left(-\log_{10}\frac{1}{\mathcal{P}_i^{(\text{link})}}\right)\right\}. \end{aligned} \tag{7.32}$$

The minimization of this quantity can be carried out using Dijkstra's algorithm. Figures 7.14, 7.15, and 7.16 present the optimum routing tree for the uplink and the downlink communications and with $q = 0.1$, $q = 0.2$, $q = 0.33$, respectively.

It can be observed from these figures that, in a random access network, the most performant topology corresponds to a star with direct communications between the medical sensors and the sink node. This can be interpreted as follows. As previously presented in Chapter 2, the wireless propagation channel of BAN is highly specific and exhibits a strong attenuation with respect to

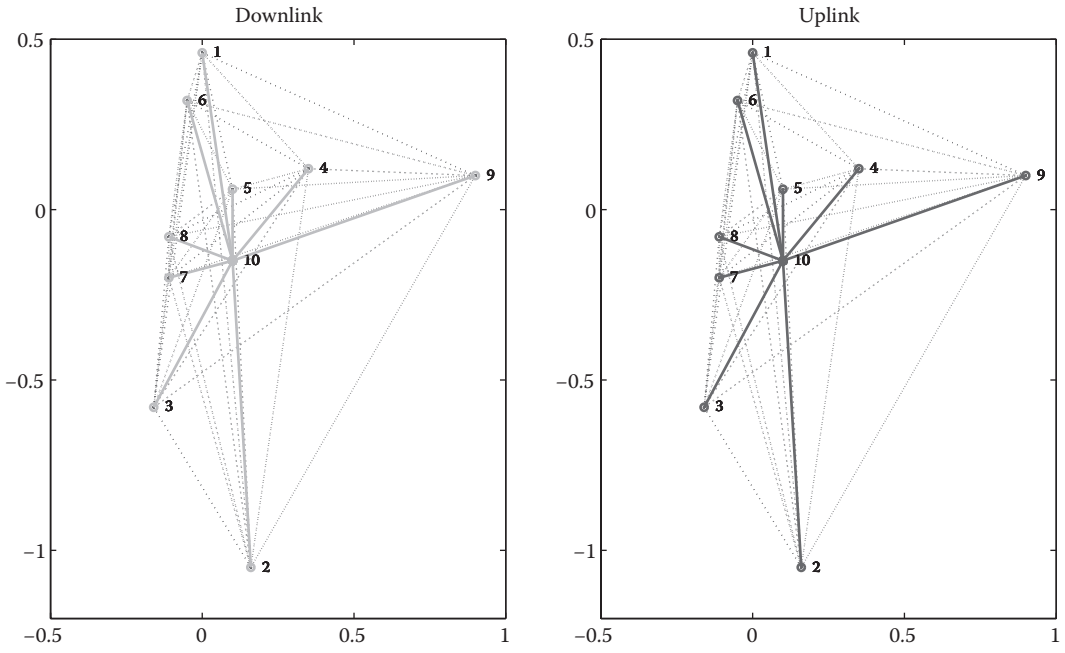

Figure 7.14 Uplink and downlink routing tree of the network in medical scenario with $q = 0.1$.

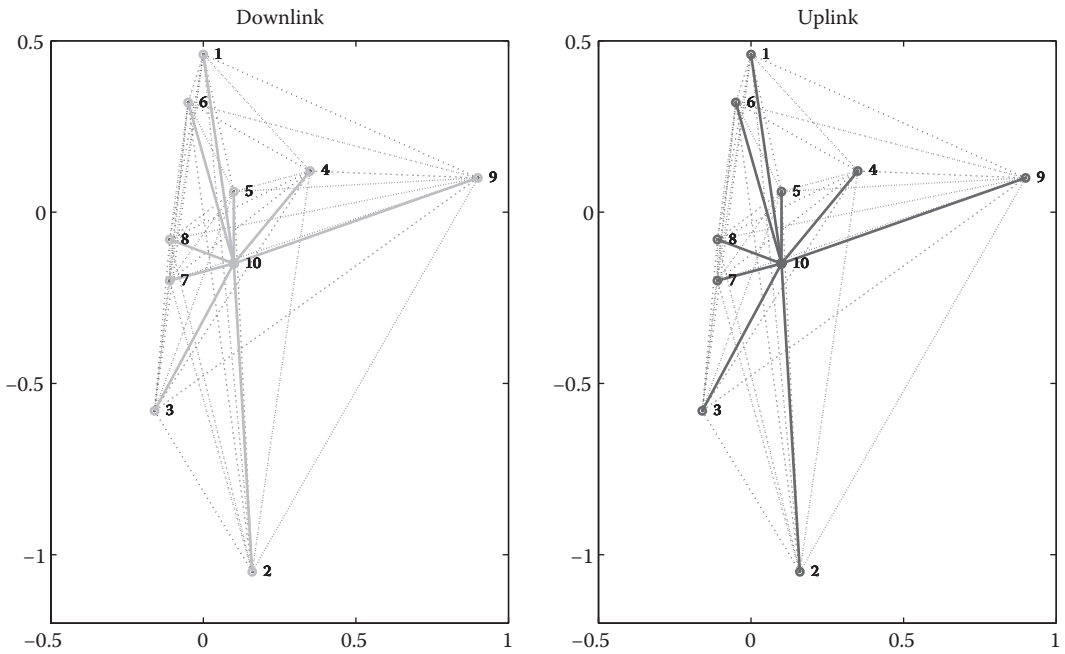

Figure 7.15 Uplink and downlink routing tree of the network in medical scenario with $q = 0.2$.

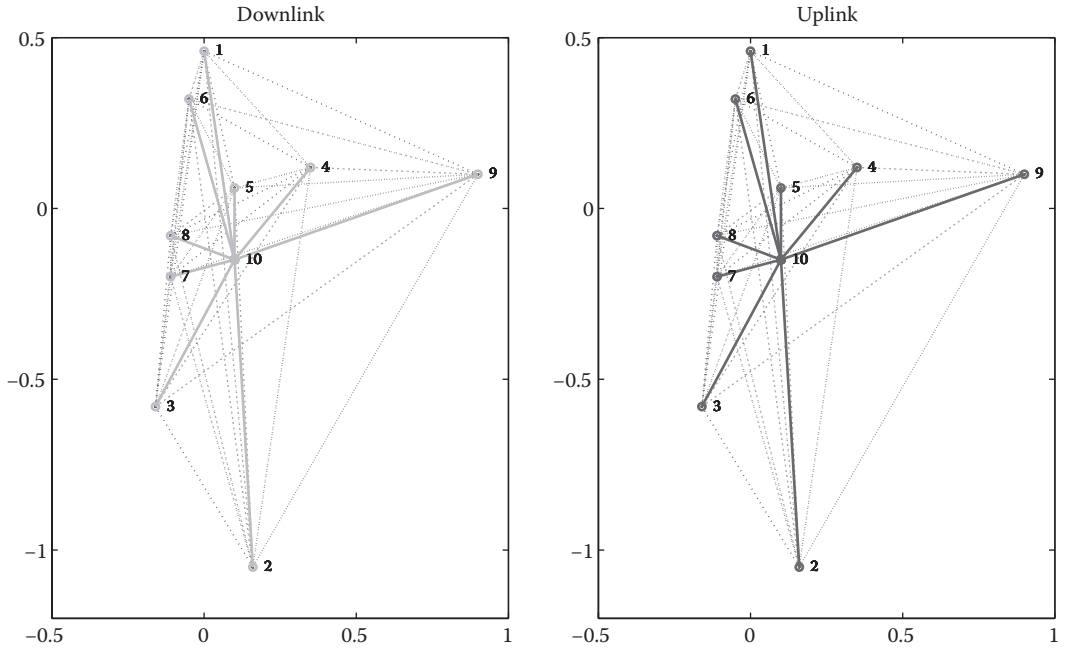

Figure 7.16 Uplink and downlink routing tree of the network in medical scenario with $q = 0.33$.

the distance. Therefore, in a noise-limited regime, far-range interferers (i.e., the nodes at a distance of $d \geq 25$ cm to the receiver) do not interfere with the emitter node of interest. Because the nodes are sparsely deployed over the body, for low values of q (which is the case due to a required high value of $\mathcal{P}_{\min}^{(\text{route})}$) the corresponding total interference on each link is low. More precisely, by recalling the definition in Equation 7.29, one has

$$\mathcal{P}^{(\text{route})} = \prod_{i}^{n_{\text{hops}}} \mathcal{P}_i^{(\text{link})} \approx \left(\mathcal{P}^{(\text{link})}\right)^{n_{\text{hops}}}$$

because $\forall i, j : \mathcal{P}_i^{(\text{link})} \approx \mathcal{P}_j^{(\text{link})} = \mathcal{P}^{(\text{link})}$. Furthermore, because the link probability of transmission is high, $\mathcal{P}_{i,j}^{(\text{link})} \approx 1$ and, finally, one has $\left(\mathcal{P}_i^{(\text{link})}\right)^{n_{\text{hops}}} \approx \mathcal{P}_i^{(\text{link})}$, which demonstrates that a multihopping strategy does not help in improving the route probability of success in the context of low rate BANs.

Finally, Tables 7.2 and 7.3 present a synthesis of the route probability of success as a function of the node medical reporting rate q and for the downlink and uplink scenarios, respectively.

7.5.5 Route Delay and Optimization of the Link–Layer Access Scheme

In the connectionless transport network, in which no traffic is induced by retransmissions, the end-to-end delay is equal to the sum of the delay on each link of the route. In an IEEE 802.15.6 BAN, and as presented in Section 7.4, two strategies can be used: random access transmissions (i.e., slotted ALOHA) and time division transmission (i.e., TDMA). Therefore, the delay of the random access network is

Table 7.2 Downlink Route Performance in a Medical Scenario

			P_{rs}		
Source Node	*Destination Node*	*Distance (m)*	*q = 0.1*	*q = 0.2*	*q = 0.33*
10	1	0.6181	0.5109	0.2453	0.0843
10	2	0.9019	0.5109	0.2453	0.0843
10	3	0.5024	0.5109	0.2453	0.0843
10	4	0.3679	0.5109	0.2453	0.0843
10	5	0.2100	0.6270	0.3866	0.1971
10	6	0.4933	0.5109	0.2453	0.0843
10	7	0.2158	0.6059	0.3595	0.1729
10	8	0.2213	0.5873	0.3362	0.2213
10	9	0.8381	0.5109	0.2453	0.0843

Table 7.3 Uplink Route Performance in Medical Scenario

			$\mathcal{P}^{(route)}$		
Source Node	*Destination Node*	*Distance (m)*	*q = 0.1*	*q = 0.2*	*q = 0.33*
1	10	0.6181	0.5186	0.2534	0.0896
2	10	0.9019	0.5314	0.2675	0.0993
3	10	0.5024	0.5314	0.2675	0.0993
4	10	0.3679	0.5314	0.2675	0.0993
5	10	0.2100	0.6398	0.4032	0.2119
6	10	0.4933	0.5186	0.2534	0.0896
7	10	0.2158	0.5942	0.3439	0.1583
8	10	0.2213	0.5772	0.3232	0.1415
9	10	0.8381	0.5314	0.2675	0.0993

$$D_{\text{ALOHA}}^{(\text{route})} = \sum_{i}^{n_{\text{hops}}} D_{\text{ALOHA}}^{(\text{i})} = \sum_{i}^{n_{\text{hops}}} \frac{1}{\mathcal{P}_i^{(\text{link})}} \tag{7.33}$$

whereas in a TDMA network with N_1 leaves and N_2 relaying nodes, it has been shown in Equation 7.28 that the average delay is deterministic and given by

$$D_{\text{TDMA}}^{(\text{route})} = \frac{N_2 \cdot N_1}{2}.$$

It can be observed from the relation in Equation 7.33 that the random access network will be highly sensitive to link impairment. For instance, let us consider that node 1 is subject to strong interference, that is, $\forall i, \mathcal{P}_1^{(\text{link})} \gg \mathcal{P}_i^{(\text{link})}$. Therefore, Equation 7.33 can be approximated as

$$D_{\text{ALOHA}} = \sum_{i}^{n_{\text{hops}}} \frac{1}{\mathcal{P}_i^{(\text{link})}} = \frac{1}{\mathcal{P}_1^{(\text{link})}} + \sum_{i \neq 1}^{n_{\text{hops}}} \frac{1}{\mathcal{P}_i^{(\text{link})}} \approx \frac{1}{\mathcal{P}_1^{(\text{link})}}$$

and, therefore, the route delay depends on the link subject to the strongest interference level. To avoid unbalancing in the links, relays can be deployed to reduce the link distance and increase the link SINR.

In Figure 7.17, a comparison between the ALOHA and TDMA route delay in a one-hop medical network is presented. It can be observed that there exists a break point that differentiates the two access strategies. More specifically, when $q \leq 0.3$, the random access scheme yields lower end-to-end delay. This is because, for low values of q, the TDMA sensing nodes spend more time waiting their turn before transmitting whereas the ALOHA nodes can transmit their data directly. On the other hand, when $q > 0.3$, the number of collisions in the ALOHA network increases due to the concurrent access by the nodes and the deterministic strategy outperforms the random strategy.

Next, it is of interest to compare between networks implementing the TDMA access scheme with or without relay nodes, that is, for $N_1 \neq 0$ and $N_2 \neq 0$. The results of the corresponding simulation are reported in Figure 7.18. As expected, the relaying nodes further increase the delay and the waiting time at low transmission rates. More specifically, the ALOHA scheme outperforms the TDMA scheme until the node probability of transmission reaches $q = 0.35$.

To summarize, as a TDMA-based scheme has a throughput $\tau = q$, it becomes very attractive for values of q beyond the maximum of the considered slotted ALOHA system, as the latter

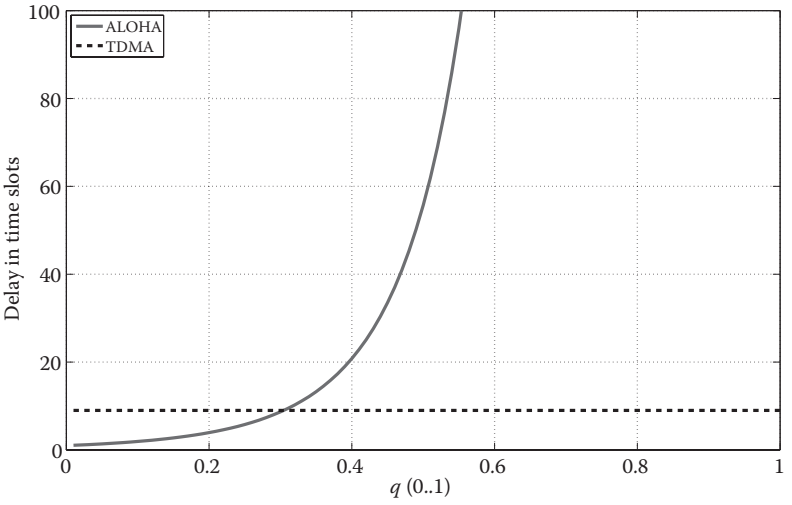

Figure 7.17 Route delay comparison of ALOHA and TDMA in a medical network.

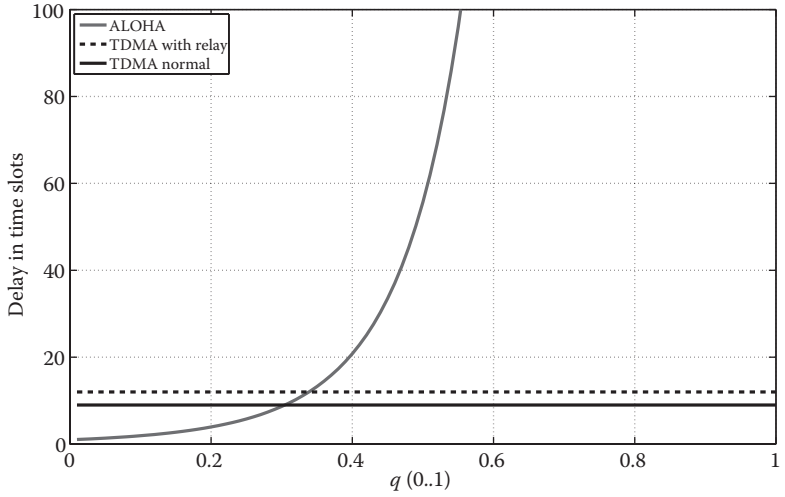

Figure 7.18 TDMA scheme with and without relay comparison in the medical network.

becomes unstable, that is, the value of the delay $D_{\text{ALOHA}} \rightarrow \infty$ because $P_s \rightarrow 0$. In scenarios with low reporting rates, the slotted ALOHA scheme is preferred.

7.6 Conclusions

In this chapter, we have investigated the performance of IEEE 802.15.6 body sensor networks under realistic propagation conditions. More specifically, we have proposed a generic analytical framework for a computation of the link probability of outage in body sensor networks subject to fading interference. The analytical derivation is built on real-life channel measurements, which allows us to accurately model the particularities of the physical propagation mechanisms found in on-body wireless transmissions—strong signal attenuation with respect to the distance and propagation through reflections off the environment.

The link-level performance analysis was conducted under two distinct medium access mechanisms: random access (i.e., slotted ALOHA) and time division multiple access (i.e., TDMA). Both strategies are part of the IEEE 802.15.6 standard and exhibit distinct advantages and shortcomings, depending on the scenario of interest. Regarding the random access approach, it is the simplest to implement and can be used for low throughput body sensor networks. The detailed performance analysis showed that the functioning region (in terms of sensor reporting rate) coincides with the requirements of most medical applications. On the other hand, when the sensor reporting rate is high or if the number of sensors increases, the TDMA strategy is preferred—even if it is more difficult to implement. Indeed, when the load increases in a random access network, the probability of collisions increases proportionally. A strictly defined time ordering of the packet sending times and silence times of each sensor is mandatory. It is important to note that the developments presented in this chapter are generic and can be used to further analyze the performance of future medical sensor networks without loss of generality.

Next, based on the link probability of outage, it has been possible to derive the optimal topology and the performance of the entire medical network. More precisely, a well-known graph

technique used in computer networks (i.e., Dijkstra's algorithm) was used to determine the optimal path between any pair of source and destination nodes. Each link was given a weight proportional to its probability of outage and the algorithm was used to determine the routes with the lowest achievable weight, that is, the highest probability of successful end-to-end transmission. A performance analysis of the routing topologies was conducted in the context of a real medical implementation. It has been observed that multihopping (the use of intermediary relay nodes) is not necessary, in general, in a medical sensor network. Moreover, the use of relays may have a detrimental effect on the end-to-end delay and would generate further interference if the random access schemes are in use.

Finally, the topology can be dynamically adapted by the network itself to meet any change in the topology (i.e., addition or removal of nodes) or in the medical reporting rate of the nodes.

Appendix A

The modeling of slow-scale fading as a log-normal distribution (i.e., a zero-mean Gaussian in decibel scale) raises mathematical difficulties, as shown in Equation 7.12. The complementary cdf of a zero-mean log-normal random variable is

$$\zeta(z;\sigma) \triangleq \frac{1}{2} + \frac{1}{2}\,\mathrm{erf}\left(\frac{-10\log_{10} z}{\sigma\sqrt{2}}\right) \tag{7.34}$$

where $\mathrm{erf} \triangleq \dfrac{2}{\sqrt{\pi}}\displaystyle\int_0^x e^{-t^2}\,\mathrm{d}t$ is the error function. The function $\zeta(z;\sigma)$ is shown in Figure 7.19 as a function of z for $\sigma \in \{4,8,12,16\}$ dB. It can be observed that $\zeta(z;\sigma)$ (i) saturates for $z \to \infty$, regardless of the value of ρ, and (ii) has the shape of a decreasing exponential function of z (for a given value of σ).

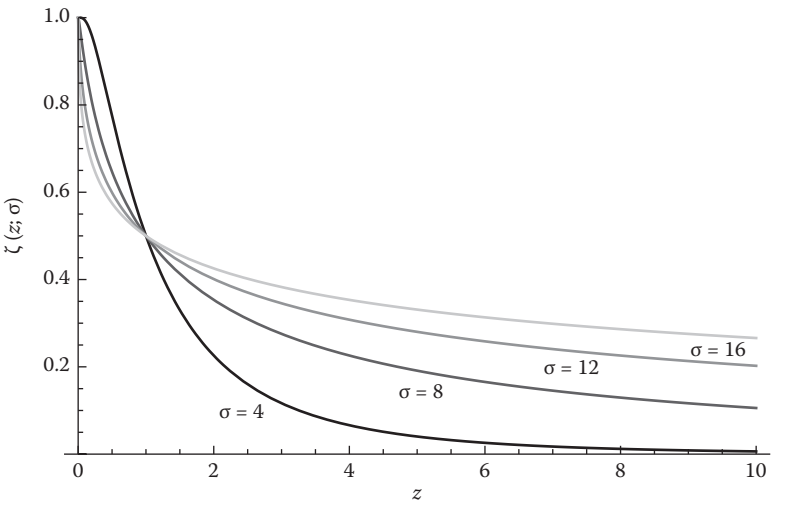

Figure 7.19 The function $\zeta(z;\sigma)$ as a function of z, considering various values of σ (in decibels).

Table 7.4 Coefficients for the Approximation of the ζ Function

	c_1	a_1	c_2	a_2	c_3	a_3	Residual
σ = 4	0.49	0.75	0.49	0.75	0.03	0.16	4.68×10^{-5}
σ = 6	0.38	0.31	0.56	1.21	0.06	0.07	4.23×10^{-6}
σ = 8	0.59	1.32	0.34	0.18	0.06	0.02	1.04×10^{-4}
σ = 10	0.29	0.09	0.65	1.17	0.05	0.01	7.53×10^{-4}
σ = 12	0.04	0	0.24	0.04	0.70	0.93	3.52×10^{-3}
σ = 14	0.20	0.01	0.03	0	0.72	0.64	1.03×10^{-2}
σ = 16	0.18	0.01	0.70	0.49	0.04	0	1.67×10^{-2}

The ζ function can be approximated with a linear combination of negative exponential functions, as in [67,68]:

$$\zeta(z;\sigma) = \sum_{m}^{\infty} c_m \exp(-a_m z) \approx \sum_{m}^{n} c_m \exp(-a_m z)$$

where the coefficients $\{c_m\}_{m=1}^{n}$ and $\{a_m\}_{m=1}^{n}$ depend on σ and can be determined in a least-squares sense with $q \geq 2n$ known points of the ζ function. The Levenberg–Marquardt algorithm [69,70] can be used to determine the coefficients $\{c_m\}$ and $\{a_m\}$ for different values of σ and 10,000 points over the interval $z \in [0,1000]$. The corresponding values are reported in Table 7.4 along with the corresponding residual sum of squares.

References

1. R. Astolfi, L. Lorenzoni, and J. Oderkirk. Informing policy makers about future health spending: a comparative analysis of forecasting methods in OECD countries. *Health Policy (Amsterdam, Netherlands)*, pp. 1–10, June 2012.
2. M. Chernew and J. Newhouse. Health care spending growth. *Handbook of Health Economics*, vol. 2, pp. 1–43, 2011.
3. United Nations Department of Economic and Social Affairs. Population ageing 2006. Wall Chart. 2006.
4. J. Xing and Y. Zhu. A survey on body area network. In *Proceedings of the 5th International Conference on Wireless Communications, Networking and Mobile Computing (WiCOM'09)*, Beijing, China, 2009.
5. E. Monton, J. Hernandez, J. Blasco, T. Herve, J. Micallef, I. Grech, A. Brincat, and V. Traver. Body area network for wireless patient monitoring. *IET Communications*, vol. 2, no. 2, pp. 215–222, 2008.
6. A. Kailas and M. A. Ingram. Wireless communications technology in telehealth systems. In *Proceedings of the IEEE Wireless VITAE Conference*, Aalborg, Denmark, May 2009.
7. D. Bhatia, L. Estevez, and S. Rao. Energy efficient contextual sensing for elderly care. In *Proceedings of the 29th International Conference of the Engineering in Medicine and Biology Society (EMBS 2007)*, Lyon, France, Aug. 2007.
8. A. Milenković and C. Otto. Wireless sensor networks for personal health monitoring: issues and an implementation. *Computer Communications*, vol. 29 no. 13–14, pp. 2521–2533, Aug. 2006.

9. O. Aziz, B. Lo, A. Darzi, G. Z. Yang. Body sensor networks, the ultimate diagnostic tool? *IEE: BSN, Wearable and Implantable Body Sensor Networks*. 2005.
10. M. J. Kane, P. P. Breen, F. Quondamatteo, and G. ÓLaighin. BION microstimulators: A case study in the engineering of an electronic implantable medical device. *Medical Engineering and Physics*, vol. 33, no. 1, pp. 7–16, Jan. 2011.
11. R. F. Yazicioglu, T. Torfs, P. Merken, J. Penders, V. Leonov, R. Puers, B. Gyselinckx, and C. Van Hoof. Ultra-low-power biopotential interfaces and their applications in wearable and implantable systems. *Microelectronics Journal*, vol. 40, no. 9, pp. 1313–1321, Sept. 2009.
12. P. Pawar, V. Jones, B.-J. van Beijnum, and H. Hermens. A framework for the comparison of mobile patient monitoring systems. *Journal of Biomedical Informatics*, vol. 45, no. 3, pp. 544–556, Mar. 2012.
13. M. R. Yuce. Implementation of wireless body area networks for healthcare systems. *Sensors and Actuators A: Physical*, vol. 162, no. 1, pp. 116–129, July 2010.
14. E. Jovanov, A. Milenkovic, C. Otto, and P. C. de Groen. A wireless body area network of intelligent motion sensors for computer assisted physical rehabilitation. *Journal of Neuroengineering and Rehabilitation*, vol. 2, no. 1, p. 6, Mar. 2005.
15. M. Yuce. Wideband communication for implantable and wearable systems. *IEEE Transactions on Microwave Theory and Techniques*, vol. 57, no. 10, pp. 2597–2604, Oct. 2009.
16. Y. Zhang and H. Xiao. Bluetooth-based sensor networks for remotely monitoring the physiological signals of a patient. *IEEE Transactions on Information Technology in Biomedicine*, vol. 13, no. 6, pp. 1040–1048, Nov. 2009.
17. M. Berg. Patient care information systems and health care work: A sociotechnical approach. *International Journal of Medical Informatics*, vol. 55, no. 2, pp. 87–101, Aug. 1999.
18. H. J. Hermens and M. M. R. Vollenbroek-Hutten. Towards remote monitoring and remotely supervised training. *Journal of Electromyography and Kinesiology*, vol. 18, no. 6, pp. 908–919, Dec. 2008.
19. T. H. F. Broens, R. M. H. A. Huis in't Veld, M. M. R. Vollenbroek-Hutten, H. J. Hermens, A. T. van Halteren, and L. J. M. Nieuwenhuis. Determinants of successful telemedicine implementations: a literature study. *Journal of Telemedicine and Telecare*, vol. 13, no. 6, pp. 303–309, Jan. 2007.
20. A. Metting van Rijn, A. Peper, and C. Grimbergen. High-quality recording of bioelectric events: Part 1. Interference reduction, theory and practice. *Medical and Biological Engineering and Computing*, vol. 28, no. 5, 1990.
21. D. Wood and D. Ewins. Comparative analysis of power-line interference between two- or three-electrode biopotential amplifiers. *Medical and Biological Engineering and Computing*, vol. 33, no. 1, pp. 63–68, Jan. 1995.
22. J. C. Huhta and J. G. Webster. 60-HZ interference in electrocardiography. *IEEE Transactions on Biomedical Engineering*, vol. 20, no. 2, pp. 91–101, Mar. 1973.
23. J. G. Webster. *Medical Instrumentation: Application and Design*. Wiley, 2009.
24. M. Fernández and R. Pallás-Areny. Ag-AgCl electrode noise in high-resolution ECG measurements. *Biomedical Instrumentation and Technology/Association for the Advancement of Medical Instrumentation*, vol. 34, no. 2, pp. 125–30.
25. A. Nonclercq and P. Mathys. Quantification of motion artifact rejection due to active electrodes and driven-right-leg circuit in spike detection algorithms. *IEEE Transactions on Biomedical Engineering*, vol. 57, no. 11, pp. 2746–2752, July 2010.
26. B. Gyselinckx, J. Penders, and R. Vullers. Potential and challenges of body area networks for cardiac monitoring. *Journal of Electrocardiology*, vol. 40, no. 6 Suppl, pp. S165–S168, 2007.
27. A. Turnbull. The use of IEC 60601-1 in supporting approvals of medical electrical devices and the role of the new collateral standard IEC 60601-1-9, ENVIRON Technical Report, no. September, 2007.
28. D.-J. Kim and B. Prabhakaran. Motion fault detection and isolation in body sensor networks. *Pervasive and Mobile Computing*, vol. 7, no. 6, pp. 727–745, Dec. 2011.
29. IEC60601-1-2, Medical electrical equipment—Part 1–2: General requirements for basic safety and essential performance—collateral standard: electromagnetic compatibility—requirements and tests. *Technical Report*, International Electrotechnical Commission, Geneva, Switzerland, 2007.

30. IEC60601-1, Medical electrical equipment—Part 1: General requirements for basic safety and essential performance, International Electrotechnical Commission, Geneva, Switzerland, 2005.
31. M. N. Nyan, F. E. H. Tay, and E. Murugasu. A wearable system for pre-impact fall detection. *Journal of Biomechanics*, vol. 41, no. 16, pp. 3475–3481, Dec. 2008.
32. K. Ni, M. Srivastava, N. Ramanathan, M. N. H. Chehade, L. Balzano, S. Nair, S. Zahedi, E. Kohler, G. Pottie, and M. Hansen. Sensor network data fault types. *ACM Transactions on Sensor Networks*, vol. 5, no. 3, pp. 1–29, May 2009.
33. J. Y. Khan, M. R. Yuce, and F. Karami. Performance evaluation of a wireless body area sensor network for remote patient monitoring. In *Conference Proceedings: Annual International Conference of the IEEE Engineering in Medicine and Biology Society*, vol. 2008, pp. 1266–1269, Jan. 2008.
34. D. Ganesan, R. Govindan, S. Shenker, and D. Estrin. Highly-resilient, energy-efficient multipath routing in wireless sensor networks. In *Proceedings of the 2nd ACM International Symposium on Mobile Ad Hoc Networking and Computing—MobiHoc '01*, vol. 1, no. 2, p. 251, 2001.
35. H. Alemdar and C. Ersoy. Wireless sensor networks for healthcare: a survey. *Computer Networks*, vol. 54, no. 15, pp. 2688–2710, Oct. 2010.
36. U. Varshney. A framework for supporting emergency messages in wireless patient monitoring. *Decision Support Systems*, vol. 45, no. 4, pp. 981–996, Nov. 2008.
37. B. Najafi, K. Aminian, A. Paraschiv-Ionescu, F. Loew, C. J. Büla, and P. Robert. Ambulatory system for human motion analysis using a kinematic sensor: Monitoring of daily physical activity in the elderly. *IEEE Transactions on Biomedical Engineering*, vol. 50, no. 6, pp. 711–723, June 2003.
38. T. Klingeberg and M. Schilling. Mobile wearable device for long term monitoring of vital signs. *Computer Methods and Programs in Biomedicine*, vol. 106, no. 2, pp. 89–96, May 2012.
39. M. Al Ameen, J. Liu, and K. Kwak. Security and privacy issues in wireless sensor networks for healthcare applications. *Journal of Medical Systems*, vol. 36, no. 1, pp. 93–101, Feb. 2012.
40. H. S. Ng, M. L. Sim, and C. M. Tan. Security issues of wireless sensor networks in healthcare applications. *BT Technology Journal*, vol. 24, no. 2, pp. 138–144, Apr. 2006.
41. S. Dağtas, G. Pekhteryev, and Z. Sahinoğlu. Real-time and secure wireless health monitoring. *International Journal of Telemedicine and Applications*, doi:10.1155/2008/135808, 2008.
42. R. Paradiso, G. Loriga, and N. Taccini. A wearable health care system based on knitted integrated sensors. *IEEE Transactions on Information Technology in Biomedicine*, vol. 9, no. 3, pp. 337–344, Sept. 2005.
43. B. Fuchs, S. Vogel, and D. Schroeder. Universal application-specific integrated circuit for bioelectric data acquisition. *Medical Engineering and Physics*, vol. 24, no. 10, pp. 695–701, Dec. 2002.
44. N. Van Helleputte, J. Tomasik, W. Galjan, A. Mora-Sanchez, D. Schroeder, W. Krautschneider, and R. Puers. A flexible system-on-chip (SoC) for biomedical signal acquisition and processing. *Sensors and Actuators A: Physical*, vol. 142, no. 1, pp. 361–368, Mar. 2008.
45. J. Van Ham and R. Puers. A power and data front-end IC for biomedical monitoring systems. *Sensors and Actuators A: Physical*, vol. 147, no. 2, pp. 641–648, Oct. 2008.
46. C. K. Ho, T. S. See, and M. R. Yuce. An ultra-wideband wireless body area network: Evaluation in static and dynamic channel conditions. *Sensors and Actuators A: Physical*, vol. 180, pp. 137–147, June 2012.
47. L. Lonys, P. Mathys, and A. Nonclercq. Human energy harvesting used for endoscopic implant power supply. In *Proceedings of Congress of the International Society of Biomechanics*, Brussels, Belgium, 2011.
48. D. Leger, V. Bayon, J. P. Laaban, and P. Philip. Impact of sleep apnea on economics. *Sleep Medicine Reviews*, vol. 16 no. 5. pp. 455–462, Oct. 2012.
49. M. R. Patel, T. H. Alexander, and T. M. Davidson. Home sleep testing. *Operative Techniques in Otolaryngology-Head and Neck Surgery*, vol. 18, no. 1, pp. 33–51, Mar. 2007.
50. M. A. King, M.-O. Jaffre, E. Morrish, J. M. Shneerson, and I. E. Smith. The validation of a new actigraphy system for the measurement of periodic leg movements in sleep. *Sleep Medicine*, vol. 6, no. 6, pp. 507–513, Nov. 2005.
51. A. Astaras, M. Arvanitidou, I. Chouvarda, V. Kilintzis, V. Koutkias, E. M. Sanchez, G. Stalidis, A. Triantafyllidis, and N. Maglaveras. An integrated biomedical telemetry system for sleep monitoring employing a portable body area network of sensors (SENSATION). In *Conference Proceedings: Annual International Conference of the IEEE Engineering in Medicine and Biology Society*, vol. 2008, pp. 5254–5257, Jan. 2008.

52. S. Chokroverty. *Sleep Disorders Medicine: Basic Science, Technical Considerations, and Clinical Aspects, Expert Consult*, 3rd ed. Saunders, Philadelphia, USA, 2009.
53. S. Quan, J. Gillin, and M. Littner. Sleep-related breathing disorders in adults: Recommendations for syndrome definition and measurement techniques in clinical research. Editorials. *Sleep*, vol. 22, no. 5, 1999.
54. S. P. Patil. What every clinician should know about polysomnography. *Respiratory Care*, vol. 55, no. 9, pp. 1179–1195, Sept. 2010.
55. C. Iber, S. Ancoli-Israel, A. Chesson, and S. Quan. *The AASM Manual for the Scoring of Sleep and Associated Events: Rules, Terminology and Technical Specifications*, 1st ed. American Academy of Sleep Medicine, Westchester, 2007.
56. J. Ryckaert, P. D. Doncker, R. Meys, A. de Le Hoye, and S. Donnay. Channel model for wireless communication around human body. *Electronics Letters,* vol. 40, no. 9, pp. 543–544, 2004.
57. S. Van Roy, C. Oestges, F. Horlin, and P. De Doncker. Propagation modeling for UWB body area networks: power decay and multi-sensor correlations. In *Proceedings of the 10th IEEE International Symposium on Spread Spectrum Techniques and Application*, Bologna, Italy, 2008.
58. S. Van Roy, C. Oestges, F. Horlin, and P. De Doncker. A comprehensive channel model for UWB multisensor multiantenna body area networks. *IEEE Transactions on Antennas and Propagation*, vol. 58, no. 1, pp. 163–170, 2010.
59. J. Takada, T. Aoyagi, K. Takizawa, N. Katayama, H. Sawada, T. Kobayashi, K. Y. Yazdandoost, H. B. Li, and R. Kohno. Static propagation and channel models in body area. In *COST 2100 6th Management Committee Meeting*, TD(08)639, Trondheim, Norway, 2008.
60. A. Goldsmith. *Wireless Communications*. New York: Cambridge University Press, 2005.
61. D. Bertsekas and R. Gallager. *Data Networks*, 2nd ed. Prentice-Hall, Upper Saddle River, New Jersey, USA, 1991.
62. J.-M. Dricot, G. Ferrari, S. van Roy, F. Horlin, and P. De Doncker. Outage, local throughput, and achievable transmission rate of body area networks. In *Proceedings of the COST 2100 Meeting*, no. TD(09) 939, Vienna, Austria, Sept. 2009.
63. C. E. Jones, K. M. Sivalingam, P. Agrawal, and J. C. Chen. A survey of energy efficient network protocols for wireless networks. *Wireless Networks*, vol. 7, no. 4, pp. 343–358, 2001.
64. Y.-A. Le Borgne, J.-M. Dricot, and G. Bontempi. Principal component aggregation for energy efficient information extraction in wireless sensor networks. In *Knowledge Discovery from Sensor Data*. Boca Raton, FL: Taylor & Francis/CRC Press. 2007.
65. S. Madden, M. Franklin, J. Hellerstein, and W. Hong. TAG: a Tiny AGgregation service for ad-hoc sensor networks. In *Proceedings of the 5th ACM Symposium on Operating System Design and Implementation (OSDI)*, Boston. 2002.
66. E. W. Dijkstra. A note on two problems in connexion with graphs. *Numerische Mathematik*, vol. 1, pp. 269–271, 1959.
67. B. G. de Prony. Essai expérimental et analytique sur les lois de la dilatabilité des fluides élastique et sur celles de la force expansive de la vapeur de l'eau et de la vapeur de l'alkool, à différentes températures. *Journal de l'École Polytechnique*, vol. 1, no. 2, pp. 24–76, 1795.
68. F. G. Lether. Elementary approximation for erf(x). *Journal of Quantitative Spectroscopy and Radiative Transfer*, vol. 49, no. 5, pp. 573–577, 1993.
69. K. Levenberg. A method for the solution of certain non-linear problems in least squares. *The Quarterly of Applied Mathematics*, vol. 2, pp. 164–168, 1944.
70. D. Marquardt. An algorithm for least-squares estimation of nonlinear parameters. *SIAM Journal on Applied Mathematics*, vol. 11, pp. 431–444, 1963.